Solid-State Protein Junctions

Mukhopadhyay, Sabyasachi; Karuppannan, Senthil Kumar; Guo, Cunlan; Fereiro, Jerry A.; Bergren, Adam; Mukundan, Vineetha; Qiu, Xinkai; Ocampo, Olga E. Castaneda; Chen, Xiaoping; Chiechi, Ryan C.

Published in:
iScience

DOI:
10.1016/j.isci.2020.101099

Publication date:
2020

iScience

CellPress
OPEN ACCESS

Article

Solid-State Protein Junctions: Cross-Laboratory Study Shows Preservation of Mechanism at Varying Electronic Coupling

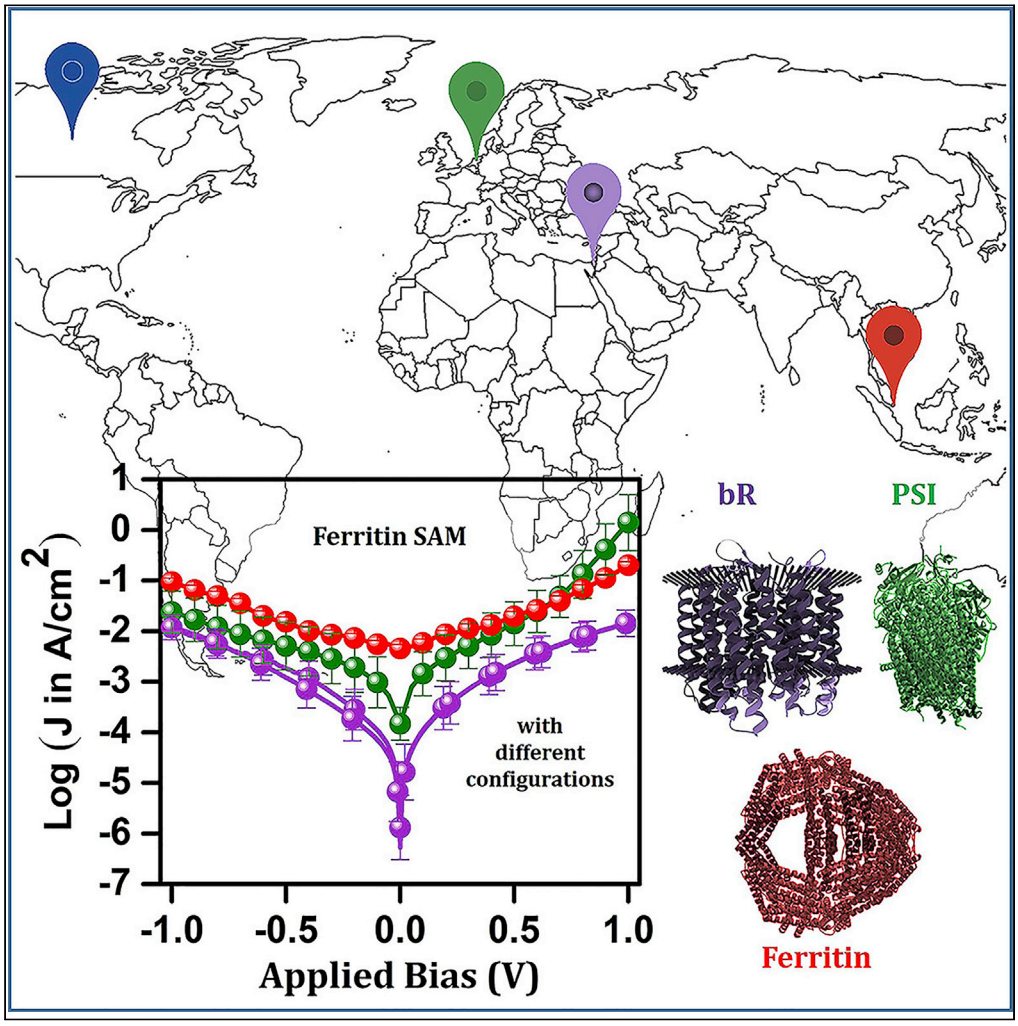

Sabyasachi Mukhopadhyay, Senthil Kumar Karuppannan, Cunlan Guo, ..., Christian A. Nijhuis, Ayelet Vilan, David Cahen

sabyasachi.m@srmap.edu.in (S.M.)
chmnca@nus.edu.sg (C.A.N.)
ayelet.vilan@weizmann.ac.il (A.V.)
david.cahen@weizmann.ac.il (D.C.)

HIGHLIGHTS

Junction geometry determines effective contact area

Mechanism of charge transport is independent of junction platform

Electrode-molecule coupling determines transport efficiency across interfaces

Tunneling dominates solid-state electron transport across protein-based junctions

Mukhopadhyay et al., iScience *23*, 101099
May 22, 2020
https://doi.org/10.1016/j.isci.2020.101099

iScience

CellPress
OPEN ACCESS

Article

Solid-State Protein Junctions: Cross-Laboratory Study Shows Preservation of Mechanism at Varying Electronic Coupling

Sabyasachi Mukhopadhyay,[1,2,9,10,*] Senthil Kumar Karuppannan,[3,9] Cunlan Guo,[1,4] Jerry A. Fereiro,[1] Adam Bergren,[5] Vineetha Mukundan,[5] Xinkai Qiu,[6] Olga E. Castañeda Ocampo,[6] Xiaoping Chen,[3] Ryan C. Chiechi,[6] Richard McCreery,[5] Israel Pecht,[1] Mordechai Sheves,[1] Rupali Reddy Pasula,[7] Sierin Lim,[7] Christian A. Nijhuis,[3,8,*] Ayelet Vilan,[1,*] and David Cahen[1,*]

SUMMARY

Successful integration of proteins in solid-state electronics requires contacting them in a non-invasive fashion, with a solid conducting surface for immobilization as one such contact. The contacts can affect and even dominate the measured electronic transport. Often substrates, substrate treatments, protein immobilization, and device geometries differ between laboratories. Thus the question arises how far results from different laboratories and platforms are comparable and how to distinguish genuine protein electronic transport properties from platform-induced ones. We report a systematic comparison of electronic transport measurements between different laboratories, using all commonly used large-area schemes to contact a set of three proteins of largely different types. Altogether we study eight different combinations of molecular junction configurations, designed so that A_{geo} of junctions varies from 10^{5} to 10^{-3} μm^{2}. Although for the same protein, measured with similar device geometry, results compare reasonably well, there are significant differences in current densities (an intensive variable) between different device geometries. Likely, these originate in the critical contact-protein coupling (~contact resistance), in addition to the actual number of proteins involved, because the effective junction contact area depends on the nanometric roughness of the electrodes and at times, even the proteins may increase this roughness. On the positive side, our results show that understanding what controls the coupling can make the coupling a design knob. In terms of extensive variables, such as temperature, our comparison unanimously shows the transport to be independent of temperature for all studied configurations and proteins. Our study places coupling and lack of temperature activation as key aspects to be considered in both modeling and practice of protein electronic transport experiments.

INTRODUCTION

A long-standing goal in (bio)molecular electronics is the development of a reliable approach to integrate proteins and peptides into electrical circuits (McCreery et al., 2013; Ratner, 2013). Understanding the mechanism of electron transport (ETp) through biomolecules in a solid-state configuration, with different device geometries, is an important step toward controlling ETp for designing bioelectronic circuits that incorporate proteins as active components.

Compared with synthetic molecules often studied in molecular electronics, proteins are much larger, which decreases the currents that pass, mostly well below what can be measured by "single-molecule" methods based on, e.g., scanning probe microscopes or break junctions. Also, as their tertiary structure may affect transport efficiency across them, the top electrode should induce no or a minimal stress to the immobilized proteins to ensure that protein structure (and orientation) on the surface can be investigated. Thus, ETp through proteins is predominantly studied in large-area configurations such as liquid

[1]Weizmann Institute of Science, Rehovot 76100, Israel

[2]Department of Physics, SRM University – AP, Amaravati, Andhra Pradesh 522502, India

[3]Department of Chemistry, National University of Singapore, 3 Science Drive 3, Singapore 117543, Singapore

[4]Key Laboratory of Analytical Chemistry for Biology and Medicine (Ministry of Education), College of Chemistry and Molecular Sciences, Wuhan University, Wuhan 430072, P. R. China

[5]Department of Chemistry, University of Alberta, 11227 Saskatchewan Dr., Edmonton AB T6G 2G2, Canada

[6]Stratingh Institute for Chemistry, University of Groningen, Nijenborgh 4, 9747 AG Groningen, the Netherlands

[7]School of Chemical and Biomedical Engineering, Nanyang Technological University, 70 Nanyang Drive, Singapore 637457, Singapore

[8]Centre for Advanced 2D Materials, National University of Singapore, 6 Science Drive 2, Singapore 117546, Singapore

[9]These authors contributed equally

[10]Lead Contact

*Correspondence: sabyasachi.m@srmap.edu.in (S.M.), chmnca@nus.edu.sg (C.A.N.), ayelet.vilan@weizmann.ac.il (A.V.), david.cahen@weizmann.ac.il (D.C.)

https://doi.org/10.1016/j.isci.2020.101099

metal (EGaIn and Hg) or ready-made contacts (lift-off float-on, LOFO or nanorods) rather than by scanning probe microscopies (especially scanning tunneling microscopy [STM] and conducting probe atomic force microscopy [AFM]) or mechanical break junctions. However, the reproducibility of experimental results of a given molecule or protein across different platforms is not really known, although former meta-data analyses could find some rough agreements for biomolecular (Amdursky et al., 2014a) and molecular junctions (Salomon et al., 2003). However, both those compilations showed in several cases significant differences between methods in the measured current densities, which is an intensive variable, and, in principle, depends on the effective electrical contact area (A_{elec}), which may be orders of magnitude smaller than the geometrical contact area (A_{geo}) of the junction, and contact resistance. Consequently, comparison of the current density derived from A_{geo} across platforms is challenging as A_{elec} depends on the details of the roughness of the molecule-electrode interfaces and the types of contacts used in the devices (Holm, n.d.; Timsit, 1982).

The mechanism of electron transport depends on how strongly the molecules are coupled to the electrodes, which affects the activation energy for transport (E_a) and/or the tunneling barrier height (ε_0), although normally one of these two energies will dominate ETp. The way molecules contact and interact with the electrodes is important, and at times critical (Moulton et al., 2003; Sayed et al., 2012). This observation that merely expresses what is well known in solid-state electronics, viz. the importance of the contact resistance. Because the contact made will likely vary between methods and possibly between the applications of a given method in different laboratories, we set out to compare ETp results (essentially, currents at given, preferably low, bias voltages) among laboratories, as obtained with different device geometries. We also compare the shape of current density, *J*-V, curves of a given protein, as measured with different junction configurations to understand how the shape of the *J*-V curve differs as a function of the protein-electrode configurations of the two contacts, required for all methods (except for junctions based on STM, which will not be considered). To establish the mechanism of charge transport across a given protein, we measured the magnitude of the current not only as a function of applied bias voltage but also as a function of temperature (*T*) to determine the activation energy (an extensive variable that does not depend on the effective contact area). We used proteins that yielded molecular films with similar thickness, i.e., imposed a similar separation between the electrodes (*d*). To get corrected current densities we further normalized *J* (= $I_{measured}/A_{geo}$)to the effective electrical contact area (A_{elec}) in different junction configurations.

Toward that end, we performed a cross-laboratory study—a first of its kind to our knowledge—aimed to compare the instruments and measurement methods and contact configurations used for electrical transport characterization at different laboratories, and to establish how the intensive and extensive (if at all) charge transport parameters change across different junction platforms, involving the University of Alberta (UoA), Canada; University of Groningen (UoG), The Netherlands; National University of Singapore (NUS), Singapore; and Weizmann Institute of Science (WIS), Israel, with standard molecular junctions as-fabricated at UoA. We conceptualized experimental studies with three different proteins, namely bacteriorhodopsin (bR), photosystem-I (PSI), and ferritin, in different device configurations, using fabrication expertise available in the different laboratories. Analyzing statistically significant numbers of *J*-V data obtained from nine different platforms, three different proteins, and *J*(V,T) data (in total we used 100–400 *J*-V curves for each type of molecular junction in our analyses; see Table S1 in Transparent), we extracted tunneling parameters, mainly energy offset/barrier height (ε_0), conductance (G_{eq}), and electronic coupling (γ) and used these results to conclude about the universal nature of the electrical transport across (bio)molecular junctions (Vilan et al., 2013; Bâldea, 2018; Xie et al., 2015; Vilan, 2017). The major conclusion is that although the extrinsic variable of current density varies greatly across platforms (due to changes in contact resistances and effective contact areas studied over a dynamic range of 8 orders of magnitude), intrinsic variables do not change; from this we conclude that the different methods probe the same mechanisms of charge transport for a given protein. The report reflects the ongoing interest and efforts in developing efficient, reliable protein-based molecular junction fabrication methods by combining top-down micro/nanofabrication with bottom-up molecular assembly.

RESULTS

Standard Molecular Junction Fabrication and Measurements

Different research groups prepare and measure molecular junctions using distinct protocols and equipment, which complicates the comparison of results of electrical characterization studies over different

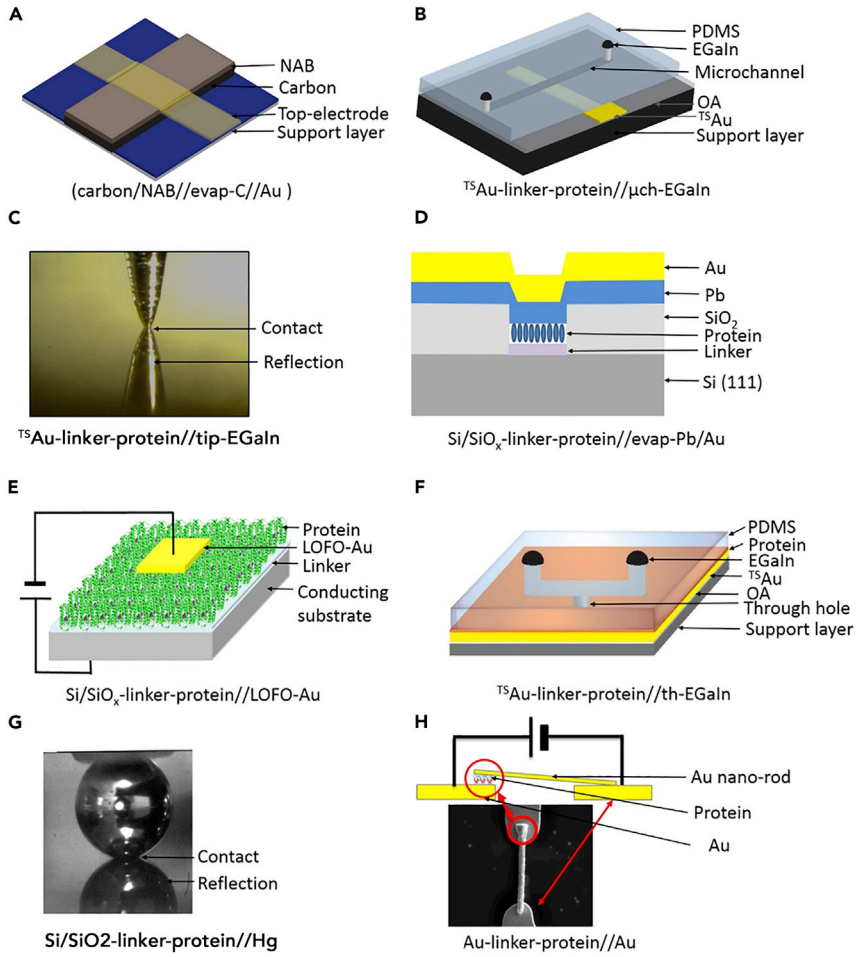

Figure 1. Illustration of the Junction Configurations Used in This Study

(A–H) (A) Carbon-NAB//e-C//Au, (B) ^{TS}Au-linker-protein//GaO_x/μch-EGaln, (C) ^{TS}Au-linker-protein//GaO_x/tip-EGaln, (D) Si/SiO_x/protein//evap-Pb//Au, (E) Si-SiO_x-linker-protein//LOFO-Au, (F) ^{TS}Au-linker-protein//GaO_x/th-EGaln, and (G) Si/SiO_x-linker-protein//Hg and (H) Au-linker-protein//Au nanowire junction. Note, "-" indicates a covalent contact, "/" indicated the interface between GaO_x and the bulk EGaln alloy or Si and SiO_x, and "//" indicates a van der Waals contact.

laboratories. As a reference standard, we choose two types of samples: (1) a sample made of carbon-NAB//e-C//Au junctions (NAB is 4-[2-(4-nitrophenyl) diazenyl]-phenyl groups; e-C is thermally evaporated carbon) and (2) a sample made of carbon-NAB (i.e., without top contact) (Yan et al., 2011). In this molecular junction, pyrolyzed photoresist film (PPF) is used as the bottom electrode, on which a ~5-nm-thick multilayer of NAB was formed via diazonium chemistry followed by deposition of a layer of carbon and then Au, both via thermal evaporation, which served as the top contact (Figure 1A). The conjugated NAB layers are highly stable, and the junctions have been proved to be highly reproducible (Sayed et al., 2012; Yan et al., 2011). To establish that all the electrical measurement equipment used in the different laboratories are the same, three samples of the type (1), each sample containing 25 junctions, were circulated and measured among the different laboratories. We also measured the current density of the sample type (2) with the tip-EGaln method to determine the ratio of A_{elec}/A_{geo}. The root-mean-square (*rms*) surface roughness of the reference sample was characterized with tapping mode AFM (see Figure S1 in Transparent Method).

The Proteins

Biomolecules exhibiting different functional properties were preferred for this study as they already represent extreme examples of efficient, long-range temperature-independent charge transport in solid-state device configurations (Castañeda Ocampo et al., 2015; Kumar et al., 2016; Ron et al., 2010). Here we compare monolayers of the following three proteins inside the junctions.

1. Ferritin is a highly symmetrical, primary intracellular, iron storage protein, which forms via self-assembly of 24 subunits. The protein shell is 12 nm in diameter with an 8-nm hollow interior and possesses channels that traverse the 2-nm-thick protein shell to allow metal ions to enter and exit. The ferritin was isolated from a hyperthermophilic archaeon *Archaeoglobus fulgidus*, which has high thermal stability (up to 80°C), making it favorable for room-temperature operation, once incorporated into solid-state devices. This type of ferritin can store up to ~7,000 Fe ions (Sana et al., 2010), but in this study we used ferritin loaded with 4,800 Fe ions (see Transparent Methods Section 1a for details procedure for iron oxide loading inside the ferritin).

2 bR is a protein-chromophore (= retinal) complex that serves as a light-driven proton pump in the purple membrane of the archaeon *Halobacterium salinarum*, a remarkably stable primordial converter of solar energy (into a proton gradient) (Jin et al., 2006, 2008)

3 PSI is a multi-subunit protein complex located in the thylakoid membranes of green plants and algae, which contains both metal atoms and photoactive molecules. It absorbs solar energy via its antenna chlorophyll molecules and transfers energy to a special chlorophyll pair, where charge separation occurs; from there, driven by a free energy slope, the electron is transported in steps to the next stage in the photosynthetic processes (Castañeda Ocampo et al., 2015; Singhal et al., 1999).

Protein Monolayer Formation

The proteins were adsorbed on the template-stripped gold surface (^{TS}Au, with glass support) or doped silicon surface (p^{++}-Si/SiO_x) either by physisorption or chemisorption via short linker molecules following previously reported methods (see Table 2 for details). We used *self-assembled monolayers* (SAM) of 6-mercaptohexanoic acid or 3-mercaptopropionic acid (MPA) on ^{TS}Au to immobilize ferritin. Ferritin was covalently bound to the linker layer utilizing carbodiimide cross-linker chemistry (EDC (carbodiimide)/*N*-hydroxysuccinimide (NHS) crosslinking reaction). For bR, we used cysteamine linker SAMs on ^{TS}Au. PSI monolayer was prepared on ^{TS}Au utilizing 2-mercaptoethanol or MPA linker followed by EDC/NHS. On p^{++}-Si/SiO_x, all the proteins were anchored via (3-aminopropyl) trimethoxysilane linker (Bostick et al., 2018). Before electrical measurements in different laboratories, protein monolayers were characterized using a variety of methods, such as AFM, ellipsometry, and infrared spectroscopy, provided in the respective references (Ron et al., 2010; Kumar et al., 2016; Castañeda Ocampo et al., 2015; Jin et al., 2008, 2006). We confirmed the monolayer quality of three different proteins on ^{TS}Au and p^{++}-Si/SiO_x substrates with tapping mode AFM measurements, which were summarized in the Supplemental Information Section 2b (see Transparent Methods Section 1a and Figures S2–S8 for more details).

The Junctions

We focus our comparison on device fabrication methods that allow for making soft contacts to surface-adsorbed protein films in a non-destructive manner, have good yields in working junctions (up to ~90%), have high reproducibility, yield statistically large numbers of *J*-V measurements, and have withstood the test of time (Castañeda Ocampo et al., 2015; Jin et al., 2008; Karuppannan et al., 2016; Ron et al., 2010). Figure 1 illustrates the various different junction platforms and methods to form the top contacts employed in this work, and Table 1 summarizes their A_{geo}, and exact composition, while throughout the text we will use shorter designations (first column of Table 1). All architectures have been used earlier and are well accepted for large-area molecular junctions (Ron et al., 2010; Kumar et al., 2016; Castañeda Ocampo et al., 2015; Jin et al., 2008, 2006). In the following discussion we summarize their preparation and unique features, focusing on their values of geometrical contact area (A_{geo}) ranging eight orders of magnitude and electrical contact area (A_{elec}) in the junctions, and surface roughness of protein-modified bottom conducting substrates and corresponding top electrodes.

EGaIn Techniques

EGaIn is a liquid-metal alloy of a Ga-In eutectic (75% Ga and 25% In by weight), which is widely used as an electronic top contact to large-area molecular junctions due to its ease in junction fabrication, non-toxicity of EGaIn, ambient stability, non-damaging nature to the monolayers, and high reproducibility of measured junction currents. EGaIn has a passivating Ga-oxide layer on the surface. The oxide layer is predominantly amorphous Ga_2O_3 with a thickness of about ~0.7 nm (at least on smooth surfaces) and is highly conducting (Kumar et al., 2016; Regan et al., 1997; Rothemund et al., 2018) and therefore adds only negligibly to the net resistance. However, the oxide skin floats on the EGaIn and behaves like a solid (resulting in non-Newtonian

Name	Junctions Description[a]	Contact Area[c] [μm^2]		
		Geometric	*Uncertainty*	*Method*[b]
LOFO-Au	Si/SiO_x-linker-protein//LOFO-Au	2 × 10^5	±10%	Img
Hg	Si/SiO_x-linker-protein//Hg	5000	±5%	Img
evap-Pb	Si/SiO_x-linker-protein//evap-Pb/Au	5000	±10%	Ptr
th-EGaIn	^{TS}Au-linker-protein//GaO_x/th-EGaIn	1000	±10%	Ptr
μch-EGaIn	^{TS}Au-linker-protein//GaO_x/μch-EGaIn	500	±10%	Ptr
tip-EGaIn	^{TS}Au-linker-protein//GaO_x/tip-EGaIn	300	±10%	Img
Au nanorod	Au-linker-protein//Au nanorod	~5 × 10^{-3}	±50%	AFM Img
NAB	Carbon-NAB//evap-C//Au	1.25× 10^5	±10%	Ptr

Table 1. Device Configurations Used in the Different Laboratories

Protein: ferritin, PSI; bR.

Img or *Ptr* mark whether the geometric area was obtained from a microscopy image (*Img*) or AFM tapping mode imaging (AFM Img) or dictated by feature patterning (*Ptr*).

[a]Refer to Figure 1.

[b]*mg* or *Ptr* mark whether the geometric area was obtained from a microscopy image (*Img*) or AFM tapping mode imaging (AFM Img) or dictated by feature patterning (*Ptr*).

[c]Refer to Figure 2.

properties), which yields a much rougher surface than, e.g., Hg, because it wrinkles. The EGaIn surface roughness is sensitive to the preparation method, but recently the effective contact areas for the different variations of the EGaIn technique have been quantified as indicated later (see for details Chen et al., 2019). Here, we used the EGaIn top electrode in the following three configurations to contact the protein monolayers on ^{TS}Au.

Tip-EGaIn. A tip-shaped EGaIn (Figure 1C) is fabricated by pulling out a microneedle of a drop of EGaIn (Cademartiri et al., 2012; Chiechi et al., 2008). The A_{geo} is determined by recording the diameter of the footprint of the EGaIn tip with the monolayer and by assuming that the footprint is circular. In this case, the tip apex is very rough due to the rupture and wrinkling of the GaO_x during the tip formation process (Chen et al., 2019). For A_{geo} larger than 1,000 μm^2, the A_{elec}/A_{geo} ratio for tip-EGaIn contacts is ~10^{-4} (Rothemund et al., 2018; Chen et al., 2019; Simeone et al., 2013; Kumar et al., 2019). Recently, it was shown that for A_{geo} larger than 1,000 μm^2 leakage current across defect can become important (Chen et al., 2019).

μch-EGaIn. The EGaIn was injected into a Polydimethylsiloxane microchannel perpendicularly aligned over an array of ^{TS}Au electrodes supporting the SAMs (Nijhuis et al., 2010a). The A_{geo}, i.e., the crossing area, was ~500 μm^2 (Chen et al., 2019; Kumar et al., 2019). The GaO_x forms *in situ* during the injection of the EGaIn in the microchannels, and therefore the GaO_x is smooth and gives about a factor of 10^2 higher A_{elec}/A_{geo} ratio for μch-EGaIn (Figure 1B) than for tip-EGaIn contacts as deduced from modeling of I-V curves, in Kumar et al. (2019), i.e., for μch-EGaIn contacts A_{elec}/A_{geo} = ~10^{-2}. The rate at which the EGaIn is injected into the channel is slow, relative to the formation rate of the GaO_x, and, given that PDMS is permeable to O_2, the GaO_x layer is continuous (Dickey, 2017; Nijhuis et al., 2010a). This device geometry may suffer from leakage currents flowing across the defects for very large values of A_{geo} >1,000 μm^2 (Jiang et al., 2015; Wan et al., 2014).

th-EGaIn. In this configuration (Figure 1F), EGaIn is stabilized in a through-hole in PDMS. The EGaIn is injected into a network of microchannels in PDMS, connected to a through-hole where the GaO_x/EGaIn is exposed and can contact the protein monolayer (Sangeeth et al., 2014; Wan et al., 2014). The bottom ^{TS}Au is non-patterned, and therefore A_{geo} is defined by the diameter of the through-hole, which was ~1,000 μm^2 for the experiments reported here. The top-contact can be placed at any place on the ^{TS}Au surface supporting the protein layer. Although this method does not suffer from electrode edges where the molecules do not pack well, the GaO_x layer is formed *ex situ* and therefore is rough due to wrinkling and handling of the EGaIn (Kumar et al., 2019). In the th-EGaIn

junction configuration, A_{elec} is very similar to that of the tip-EGaIn method ($A_{elec}/A_{geo} = 10^{-4}$) (Kumar et al., 2019; Sangeeth et al., 2016; Wan et al., 2014). The second and third setups can both be used for temperature-dependent studies.

Junctions with Si/SiO$_x$ Bottom Electrodes

LOFO-Au. In this "lift-off, float-on" (LOFO) method (Haick and Cahen, 2008; Vilan and Cahen, 2002), the top contact was prepared by deposition of ready-made Au pads onto the protein film from a liquid (Figure 1E). The pads float on water, into which the Si substrate, covered with regrown <1.0-nm SiO_x, supporting the protein monolayer was immersed. The value of A_{geo} was 2×10^5 μm^2, and its inner, glass-stripped surface has an average *rms* roughness of <1 nm (1.0 μm × 1.0 μm AFM scan area) (Mukhopadhyay et al., 2015). LOFO is a low-pressure, low-temperature method that works well for water-compatible molecules such as proteins and is vacuum compatible, as required for low-temperature measurements (Sepunaru et al., 2012). Its major disadvantage is the non-negligible skill required to prepare these contacts; in addition, adventitious materials from the ambient environment are present on the electrodes, which can reduce the work function and/or limit electrode-protein coupling (Reus et al., 2012). This method was used for temperature-dependent studies.

Hg Drop. The protein monolayers were contacted with a hanging drop of Hg (Figure 1G) (Ron et al., 2010; Haick and Cahen, 2008). This method was used for room-temperature measurements only. The A_{geo} is ~5,000 μm^2 as determined optically from the diameter of the circle made by the Hg drop onto the surface. The high surface tension of Hg (the contact angle between Hg and an alkyl monolayer is 150°) (Seitz et al., 2006) implies that Hg follows the large surface terrain, and A_{elec} is determined by the roughness of the protein layers on the Si/SiO_x substrate.

evap-Pb/Au. The top contact was made by direct evaporation of lead (Pb) on the protein layers via a shadow mask (Figure 1D). Pb can be vacuum evaporated under very mild (low-temperature) conditions. This method, demonstrated earlier for organic molecules with an exposed labile group (Yu et al., 2014) was used to contact bR protein films on Si/SiO_x substrate. The contact area, defined by a shadow mask, is ~5,000 μm^2. Here, we can only assume that Pb layer forms continuous and conformal contact with the protein monolayer. In principle, such contacts might be transferable to future practical devices.

Au-Nanorod Junction. Au-nanorod junction (Figure 1H) of Au-linker-protein//Au was made by dielectrophoresis trapping of Au nanorods between two *micropatterned* Au leads on a *silicon substrate;* the protein SAM is adsorbed on the micropatterned Au leads connected to external electronics. Although both ends of the nanorod contact a protein layer, one end is always shorted, yielding a single active molecular junction (Guo et al., 2016; Yu et al., 2015). The geometrical contact area for nanorod junction is a narrow rectangle with length dictated by the overlap between the nanorod and the protein-covered Au lead (500–2,000 nm long); its width is defined by the rod's diameter (200 nm) reduced to only 10–20 nm, due to curvature. In contrast to spherical liquid contacts (EGaIn and Hg), the solid nanorod does not flatten by adhesive forces. Therefore the geometrical contact area for nanorod junction has both significant junction-to-junction variation (varying rod-pad overlap) and large uncertainty (curved contact); as a rough estimate it is set to 5,000 nm^2(Guo et al., 2016). Electrical measurements with this method were restricted to 0 ± 0.5 V range to avoid damage due to junction heating.

Effective Contact Area of the Biomolecular Junctions

The "bottom" contact is always the conductive substrate on which the proteins were adsorbed. Fabrication of the "top" contact is challenging, as it must not damage the soft protein material. As mentioned in the Introduction, determining the value of A_{elec}, or how many molecules contribute in parallel to the measured current, is a major challenge in molecular electronics on ensembles of molecules. Figure 2 shows schematically the difference between A_{geo} and A_{elec}. The A_{geo} refers to the macroscopic dimension of the overlap between the bottom and top electrodes, as determined by imaging or patterning. In practice, however, surface roughness limits the value of the A_{elec} to a rather small fraction of the A_{geo}. The value of A_{elec} can be up to 2 to 6 orders of magnitude smaller than the A_{geo} for contacts between two solid-state electrodes or a solid and liquid electrode material (Holm, n.d.; Timsit, 1982). Although this issue is recognized also in molecular junctions (Cademartiri et al., 2012; Nijhuis et al., 2010b; Rothemund et al., 2018; Salomon

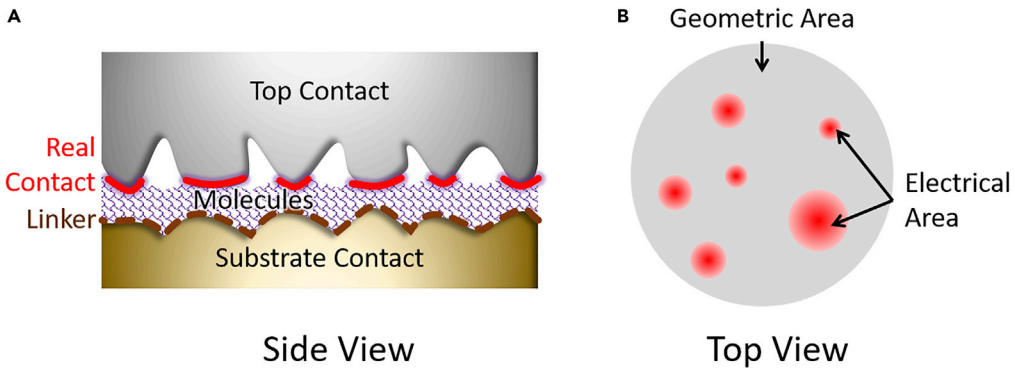

Figure 2. Geometric vs. Electrical Contact Area

(A) Schematic illustration of the side view of the junction shows how the roughness in the bottom and top contacts results in $A_{elec} << A_{geo}$ leaving room for air (in experiments performed in ambient environments) or vacuum (for experiments performed under reduced pressure); red lines indicate A_{elec}.

(B) Top view illustrates that the junction is a collection of few contact points in parallel as indicated by fuzzy red regions.

et al., 2003; Simeone et al., 2013), it has been only rarely experimentally determined. In this report, we verified the value of A_{geo} for all techniques, and, therefore, all current density values reported here are based on the relevant A_{geo} values. Nonetheless, we will argue that A_{geo}/A_{elec} variations for junction to junction originates in our inability to know, let alone control, the A_{elec}, with the exception of EGaIn top electrodes for which the ratio (A_{geo}/A_{elec}) is statistically known (and has been used before to rationalize the differences in current density measured across molecular junctions using different platforms) (Chen et al., 2019; Sangeeth et al., 2016).

Electrical Characterization

Room-temperature charge transport measurements were carried out in ambient conditions. For statistical analysis, 100–400 *J-V* traces were obtained from 20–30 molecular junctions, which were then used to determine the log-average *J-V* curves and log-standard deviation following previously reported methods (see Section A3 and Table S1 in Transparent Method). Temperature-dependent transport measurements were carried out with th-EGaIn and LOFO-Au junctions (see Table 1 and Figure 1) in temperature-controlled cryogenic probe stations (pressures varied between $\sim 10^{-6}$ and 3×10^{-5} mbar). The currents across the junctions did not change upon changing the pressure from ambient to vacuum, which indicates that the contacts were stable at low pressure also (see section A4 in Transparent Method). The devices were slowly cooled, and their *J-V* characteristics measured at intervals of 5 K (GaO_x/th-EGaIn junctions) and 10 K (LOFO-Au junctions), allowing the devices to stabilize before performing each scan.

DISCUSSION

Calibration by "Standard" Molecular Junction

Different research groups prepare and measure MJs using distinct protocols and equipment, which complicates the comparison of the results of electrical characterization studies over different laboratories. As a reference junction, we choose carbon-NAB//e-C//Au as this junction is robust and stable and can be readily shipped. This reference molecular junction had a value of A_{geo} of 1.25×10^5 μm^2 (Figure 1A; for details see Supplemental Information Sections A2a and A3a) and was measured in all the participating laboratories, starting with its "home," in Edmonton (UoA, Canada); followed by WIS, Israel; NUS, Singapore; and UoG, The Netherlands. Figure 3 shows a semi-log plot of the *J-V* traces measured in the different laboratories, where 1 to 4 mark the order of measurement. Overall, the reproducibility between the different laboratories is good, with some time degradation at the high-voltage range, likely due to changes in the probe/PPF contact resistance with time (fully encapsulated NAB junctions last for years without change). This result establishes that the electronic measurement systems between the laboratories are comparable. We note that the *J-V* of Figure 3 was measured using only two probes because the biomolecular junctions could only be measured in 2-probe configurations (molecules were sandwiched between electrodes). Still, we note that if moderately conducting leads, such as the carbon-based electrodes in this reference device, are used, they are better characterized by four probes to eliminate the series resistance contribution.

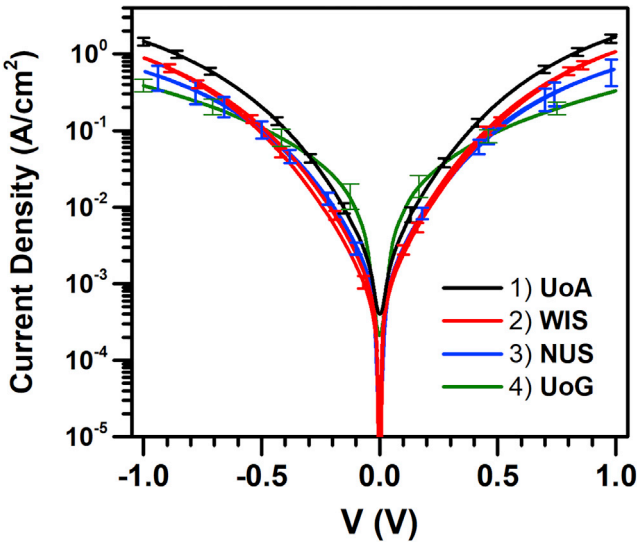

Figure 3. Validation of Measurement Equipment

Current density (A/cm^2) (on log scale) versus voltage (V) curves for carbon-NAB (5 nm)//e-C(10nm)/Au(15 nm) junctions, measured in different laboratories. The error bars represent the standard deviations in current densities over ~140 traces. We collected a similar number of *J-V* traces from the same junctions at different laboratories.

As an additional control, the current density across a reference sample of carbon-NAB (i.e., lacking the carbon-Au top contact) was also measured with tip-EGaIn in direct contact with NAB (i.e., carbon/NAB// GaO_x/tip-EGaIn junctions) with an A_{geo} of 3.8 × 10^3 μm^2. For this junction, the current density was ~3.5 orders of magnitude lower (see section A3a and Figure S9) than for the junctions shown in Figure 3, an effect that overwhelms the above-mentioned increase in contact resistance with time. This difference is very similar to the 4 orders of magnitude difference between the A_{eff} and A_{geo} due to the roughness of the electrodes (i.e., the ratio A_{elec}/A_{geo} is 10^{-4}) as illustrated in Figure 2; A factor of 10^{-4} was also reported by the group of Whitesides (Rothemund et al., 2018; Simeone et al., 2013) and confirmed by the group of Nijhuis (Chen et al., 2019; Sangeeth et al., 2014; Yuan et al., 2018), which is attributed to the surface roughness of the cone-shaped tips (tip-EGaIn) (Chen et al., 2019).

Protein Monolayer Characterization

Before considering the transport characteristics across the different platforms and laboratories, we determined the quality of the protein films, prepared by each laboratory, as shown in Table 2. From AFM or ellipsometry, the thicknesses of the monolayers of ferritin, bR, and PSI layers were comparable with the size of the corresponding single proteins, indicating the formation of well-packed protein monolayers. However, the monolayer coverages vary among different laboratories as prepared by different methods or linker molecules. Each protein-SAM was analyzed by tapping-mode AFM imaging from which we calculated the protein surface coverage as well as *rms* surface roughness from the AFM topography over an area of 1 μm^2 (see Section A2b and Figures S2–S8). The *rms* surface roughness of the self-assembled protein surfaces on the bottom electrode changes from 0.5 nm (for ^{TS}Au or Si/SiO_x substrates) to 1.3–2.7 nm (Table 2), which could also lead to variation in the ratio A_{elec}/A_{geo} over the different platforms. The surface coverage of ferritin monolayers ranges from ~40% to ~95%, that of bR films is from ~60% to ~95%, and that of PSI monolayers is from ~50% to ~80%. Such differences can originate from the grade of chemicals used, environments, and person-to-person variation in fabrication methods. Based on earlier work (Castañeda Ocampo et al., 2015), the differences in monolayer coverages affect the measured current magnitudes by at most a factor of 2–3, which can explain the results shown later (Figure 4). Given the spread between *J-V* on the same protein junctions (which can reach up to an order of magnitude), we can ignore variations in the monolayer coverages across the different laboratories (Table 2).

Room-Temperature Current Density-Voltage (*J-V*) Characteristics

Figure 4 summarizes the room-temperature *J-V* characteristics of the junctions made with the different proteins, bR (Figure 4A), ferritin (Figure 4B), and PSI (Figure 4C), in different laboratories. The legend lists the

Protein	Substrate	Linker[a]	Lab	Protein Thickness (nm; ±1)	Roughness[b] (nm; ±0.1)	Coverage (%; ±5)
bR	^{TS}Au	6-Amino-1-hexanethiol	NUS	7	1.3	65
		Cysteamine	NUS	7	1.6	60
		Cysteamine	WIS	7	1.6	95
		Cysteamine	UoG	8	3.2	65
	Si/SiO_x	(3-Aminopropyl) trimethoxysilane	WIS	7	2.3	85
Ferritin	^{TS}Au	6-Mercaptohexanoic acid	NUS	7	2.0	50
		3-Mercaptopropionic acid	WIS	5	2.6	60
		6-Mercaptohexanoic acid	UoG	7	2.8	65
	Si/SiO_x	(3-Aminopropyl) trimethoxysilane	WIS	7	1.4	95
PSI	^{TS}Au	3-Mercaptopropionic acid	NUS	7	1.4	80
		2- Mercaptoethanol	WIS	7	2.4	95
	Si/SiO_x	2- Mercaptoethanol	UoG	7	2.1	80
		(3-Aminopropyl) trimethoxysilane	WIS	8	2.8	60

Table 2. AFM Analysis of the Protein Films Prepared by the Different Laboratories

[a]See Supplemental Information, Section SA2b and Figures S2–S8 for further detail.

[b]Roughness value is the *rms* roughness over the scanned area of 1 μm^2.

different configurations and laboratories that prepared them (as summarized in Figure 1, Table 2, and Figures S10 and S11 and section A3b for measurement details to specific device configurations) (Castañeda Ocampo et al., 2015; Garg et al., 2018; Kumar et al., 2016; Rothemund et al., 2018; Vilan et al., 2017; Wan et al., 2014). The I-V data for Au nanorod junctions are shown on Figure 5, and will be discussed separately.

The bR junctions yield rather reproducible current densities, as shown in Figure 4A, where all *J-V* curves are within error from one another; the only exception is the tip-EGaIn junction, which yields a few orders of magnitude lower nominal current density (Cademartiri et al., 2012; Chen et al., 2019; Nijhuis et al., 2012; Rothemund et al., 2018). Once corrected for the ratio A_{elec}/A_{geo} of 10^{-4}, all data fall within one order of magnitude (Figure S12 in section A3b).

In few tip-EGaIn junctions we observed rectification, with rectification ratios of up to 50, whereas those junctions with μch-EGaIn and th-EGaIn top contacts did not rectify significantly (Table S2). We ascribe this to the fine details of the SAM//EGaIn contact, which, in the experiments with tip-EGaIn, result in a large potential drop at the SAM//EGaIn interface relative to the Au-SAM interface, leading to rectification (Kumar et al., 2019).

The current densities across ferritin (Figure 4B) fall in two distinct ranges, with roughly the same 10^4 factor between them (see also Figure S12B). Generally, each mode of EGaIn was prepared by a different laboratory. To verify that the much lower current density of tip-EGaIn is not due to human operation, two laboratories prepared tip-EGaIn contacts to ferritin: UoG and WIS; the resulting *I-V* curves (Figure 4) are fairly reproducible between them, and the different bias windows did not affect the measurements. In

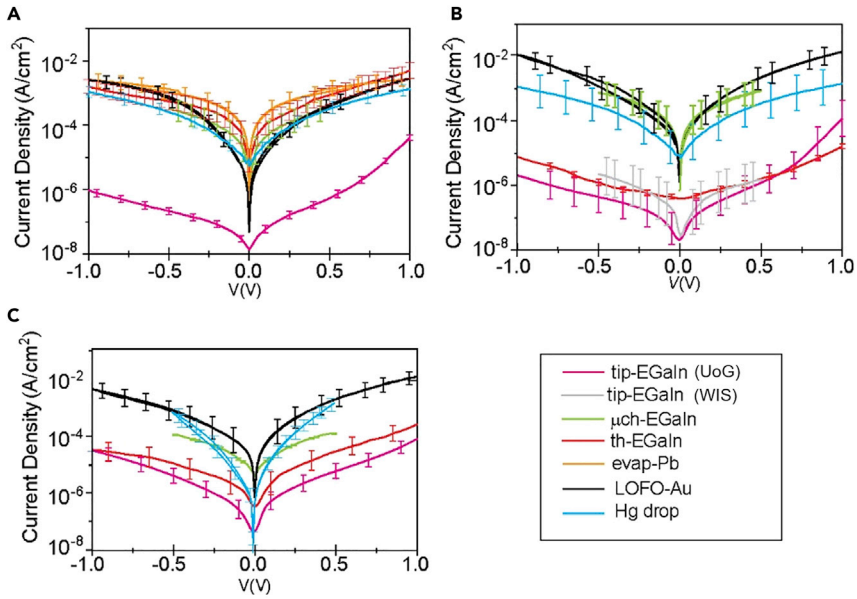

Figure 4. Protein Junction Transport Results at Room Temperature

(A–C) Current density (A/cm^2) versus voltage (*J-V*) data for different junction configurations with (A) bR (B) ferritin, and (C) PSI. The tip-EGaIn junction measurements were reproduced at WIS (gray) and UoG (magenta), showing the reproducibility between the different laboratories (B). Error bars represents statistical variations in current densities over measured *I-V* traces for different devices (as in Table - S1)

comparison, the WIS-prepared μch-EGaIn has ~10^4 higher current than the tip-EGaIn prepared by the same laboratory. The th-EGaIn contact (red curves in Figure 4) represents an interesting case: when it contacts bR, it yields a high current density, similar to the majority of top contacts; however, the same contact to ferritin yielded a low current density, similar to that of tip-EGaIn and in agreement with previous findings for n-alkanethiolate SAMs (Wan et al., 2014). This can be understood if globular ferritin produces significant roughness by its own (see Table 2). For the tip-EGaIn and th-EGaIn the top electrode, along with the GaO_x layer, is formed *ex situ*, and thus the GaO_x layer wrinkles and buckles during handling, which lowers A_{elec}. In contrast, the μch-EGaIn top contact, along with the GaO_x layer, is formed *in situ* for which the A_{elec} increases considerably by about 10^2 times (Jiang et al., 2015). We postulate that because the *ex situ*-formed oxide of th-EGaIn is confined in a through-hole, it is too rigid to adapt to the protein roughness, and therefore the current density via th-EGaIn is more sensitive to the roughness and mechanical properties of the bottom substrate than other types of contacts. Unlike tip-EGaIn, which can easily deform and release pressure (Rothemund et al., 2018), th-EGaIn cannot yield due to this confinement, and therefore this top electrode may result in exerting a significant pressure on the monolayer during the formation of the top contact.

Finally, the current density across PSI (Figure 4C), based on A_{geo}, showed the smallest net spread in current densities. However, after correcting for the differences in A_{elec}/A_{geo} for the different junction configurations (see Figure S12C), the spread is similar to that obtained for ferritin and bR, especially if single outlier curves are excluded.

Role of the Linker

Several linker molecules were used to achieve reproducible SAM of the examined proteins. On Si the linker was identical for the three tested proteins, whereas linkers to Au were adjusted to the protein's chemical structure, electrostatic charge distribution of protein surfaces, and methods of preparation. As reported in Table 2, apart from a few exceptions, the linker was identical for each protein. Importantly, the SAM quality was similar between the different laboratories, supporting the choice of linker for each protein. Although Table 2 shows variability in binding density and roughness, there is no correlation between these structural characterizations and the net current of Figure 4, which, for the protein density on the substrate surface, confirms earlier results (Castañeda Ocampo et al., 2015). The role of the linker was directly tested in two occasions (see Figure S13 in secti).

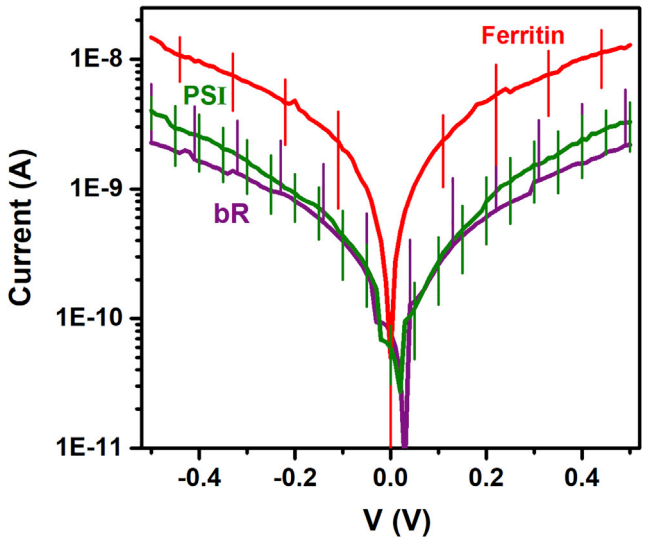

Figure 5. Transport Results for Gold Nanorod Junctions Experimentally Measured Currents versus Applied Bias for Junctions Fabricated with Gold Nanorod on Protein SAM on Patterned Gold Electrodes (At Room Temperature)

Average currents were obtained from at least 10 different junctions where error bar represent variation of measured currents over junctions. 10^{-10}A corresponds to ~2 A/cm^2 (cf. Table 1).

Such comparative experiments are reported here for completeness' sake; their results do not alter the general picture.

Role of Protein Orientation

The arrangement or orientation of the proteins on a gold/Si substrate and their structural and dynamic properties have been simulated using molecular dynamics studies as reported (Boussaad and Tao, 1999; Tao, 2006; Waleed Shinwari et al., 2010). Modification of electrodes with linker molecules eliminates unpredictable orientations of proteins on the electrode surface, because then the proteins can bind to the linkers via specific (bioengineered) positions. An appropriate choice of linker molecules can alter protein orientation in a controlled fashion (Gaigalas and Niaura, 1997; Schnyder et al., 2002)—as we have done here for PSI (Castañeda Ocampo et al., 2015) and bR (Jin et al., 2006), based on our previous reports—and thus reduce unknowns in the junction structure related to the orientation of the protein. An extensive study on cytochrome *c*, with wild-type and seven mutants of the included cysteine for directed binding to the substrate, showed at most four times difference in currents at 0.05 V (Amdursky et al., 2014b). When proteins are attached to substrate surfaces through an organized monomolecular layer with site-specific immobilization, it provides better reproducibility and better control over electron transfer and transport measurements than approaches based on physisorption of proteins on surfaces. Relevant to our study reported here, we have explored a detailed comparison with PSI, where protein orientation was altered by varying the organic linker molecules (see Figure S13 in section A3b) on ^{TS}Au substrates, and a 3-fold change in current was observed between the two orientations (Castañeda Ocampo et al., 2015). Although certainly significant, this effect is much smaller than what we measure here between different junction contact configurations, i.e., in comparing junctions between different metal/protein/metal configurations, we will neglect the effect of different linker molecules. The effects related to the orientation are not applicable for ferritin given its globular tertiary structure. For bR we have shown that the orientation is always directional with the linkers used in the present study. For these reasons, the orientation of the proteins in the junction plays only a minor role in the measured currents in the present study Figure S13 in Section SA3b and detailed discussion in Section SB1.

Top Electrode Effects

When comparing normalized current densities, the above-mentioned issue of A_{geo} versus A_{elec} is always a problem, and *the issue appears most pronounced in the range between nanoscopic and macroscopic*

areas (Cademartiri et al., 2012; Simeone et al., 2013). In the following we point to some of the differences between the contact methods, relevant to this issue.

Comparison of EGaIn Techniques

Because in "μch-EGaIn" the liquid metal is actively pushed against the protein and confined in small channel, its ability to yield and deform is limited, which might well result in some pressure on the protein film (similar to the gravity push in the Hg drop configuration). In tip-EGaIn junctions the alloy exerts negligible pressure on the proteins (as suggested by AFM measurements on EGaIn tips Chen et al., 2019). The th-EGaIn junctions differ from the μch-EGaIn ones in that in the former the GaO_x layer is formed *ex situ*, and in the latter *in situ*, which is therefore smooth (and, as mentioned earlier, gives ~2,000× larger A_{elec}) (Kumar et al., 2019). In terms of pressure, EGaIn that is injected in hole-modified microchannels (th-EGaIn) will likely also exert negligible pressure on the proteins (although shear pressure may become an issue at extremely large flow rates).

The LOFO-Au Method

This method (Figure S11) uses the peeled (and thus smoother) side of the metallic film, which was measured to have *rms* ~1.0 nm over a 10 × 10 μm^2 area (Mukhopadhyay et al., 2015) as its active surface. The interface is then formed by repulsion of the floating solvent, which may lead to wrinkling of the metallic leaf. Such wrinkling introduces long-range corrugation of the top electrode interface, an annoying feature that, though, is unlikely to change A_{elec} by even one order of magnitude. Another effect can be due to the physisorption of the leaf from the solution on the protein surface, viz. trapped pockets of solvents that prevent direct Au-protein contact after drying can lower A_{elec} (Vilan and Cahen, 2002).

Evaporated Contact

The electrode/protein contact should be less of an issue by using low-temperature metal evaporation, possible with Pb (or Bi), which was shown to work well on an organic molecular monolayer (Lovrinčić et al., 2013). The roughness of the Pb top electrode will be a convolution of the roughness of the protein monolayer, which is ~2.5 nm (Table 2), and the granularity of the metal. Judging from transmission electron microscopic cross-sectional images (unpublished data) the latter can decrease the contact area by a single-digit factor.

With the Hg drop method (Figure S10 in section A3b), the seminoble metal might be expected to follow the roughness of the protein monolayer, but Hg's high surface tension does not make that possible on a scale of nm-s.

For all these larger top contact area methods, LOFO-Au, Hg, EGaIn, and evap-Pb, the A_{elec}/A_{geo} ratio is within 2 orders of magnitude, a range that also reflects that th- and tip-EGaIn have larger macroscopic roughness than the other methods.

Nanoscopic, Pure Metal Junctions

Figure 5 shows averaged I-V curves for the three proteins contacted by Au nanorod technique. It differs in the following two main aspects from all the above-mentioned techniques: (1) it includes no oxide layer compared with GaO_x in EGaIn contacts and SiO_x for Si substrates and (2) its geometrical contact area is at least ~ 10^5 smaller than the above-mentioned configurations (see Table 1). Because of the uncertainty in the exact contact area of nanorod junctions, Figure 5 shows current (in A) rather than current-density (A/cm^2). This comparison shows similar currents for PSI and bR proteins and almost 10-fold higher current for ferritin. We could attribute the higher conductance for the iron-loaded ferritin protein cage to the strong electronic coupling between Au-ferritin (iron)-Au configuration.

Temperature-Dependent Transport Measurements

To elucidate the transport mechanism across the proteins for each device configuration, we measured junction current density as a function of temperature (Figure 6). We compare the temperature-dependent current density of protein films with th-EGaIn (reddish traces in panels A–C/red symbols in panels D–F), μch-EGaIn (green symbols in panel F), and LOFO-Au (bluish traces in panels A–C/blue symbols in panels D–F), for the three different proteins (see section A4). The three top panels show that the directly measured current varies only mildly with the applied temperature, much less than the magnitude change induced by the contacts. The latter explains the use

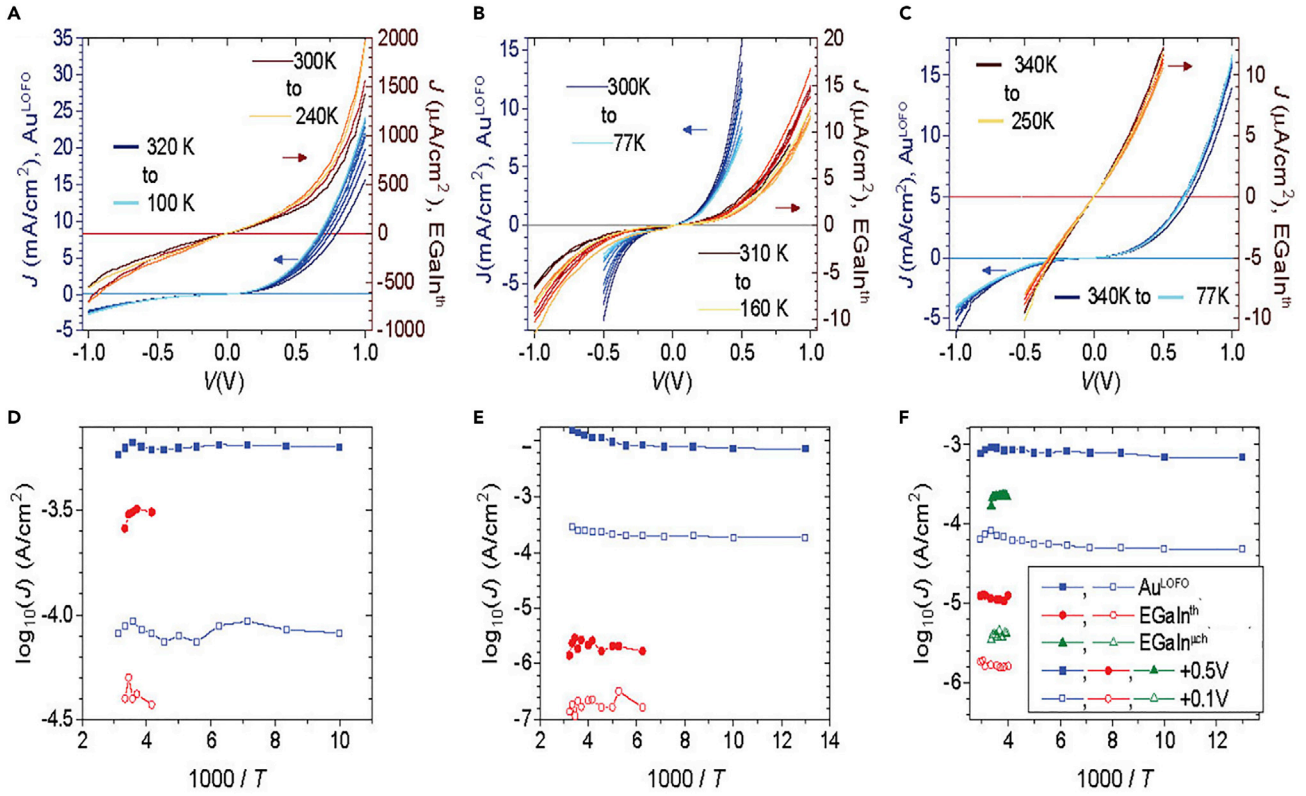

Figure 6. Temperature Dependent Transport across Solid-State Protein Junctions

Temperature-dependent *J-V* characteristics of junctions with (A, D) bR, (B, E) ferritin, and (C, F) PSI, showing the direct *J-V* response (A–C) and their Arrhenius plots (D–F) for values of *J* measured at +0.5 V (filled symbols) and +0.1 V (hollow symbols). The plots show two electrode configurations: Si/SiO_x-protein//LOFO-Au (bluish traces, left y axis in top panels, blue symbols in bottom panels), ^{TS}Au-protein//μch-EGaIn (green symbols in bottom panels), and ^{TS}Au-protein//th-EGaIn (reddish traces, right –y axis in top panels, red symbols in bottom panels).

of separate y axis in panels (A–C), and it originates in different A_{elec} to A_{geo} ratios, as explained in the former section. Here we have the opportunity to investigate whether the activation energy—an extensive parameter that is independent of A_{elec} and A_{geo}—depends on the device configuration, as done in the three lower panels of Figure 5. Here, we plot current density values at bias voltages of 0.1 V (Figures 5D–5F, hollow symbols) and 0.5 V (Figures 5D–5F, filled symbols) versus (1,000/T), i.e., an Arrhenius plot.

The results show that charge transport across the junctions formed with th-EGaIn top electrodes is temperature independent for all the proteins used in this study (Garg et al., 2018). For the Si/SiO_x-linker-ferritin//LOFO-Au junctions, log(*J*) at +0.5 V decreases from −1.80 to −2.13, which may be due to occluded and surface charges of the Si oxide on the clean Si surface (Garg et al., 2018). Therefore, the most straightforward interpretation of these results is that transport across all the junctions is dominated at all temperatures by a temperature-independent charge transport process; the one mechanism that could fit this behavior is quantum mechanical tunneling. Note that this temperature-independent charge transport behavior does not necessarily imply that all the transport is tunneling, but that quantum mechanical tunneling is the dominant process, the rate-determining (current is a rate) step (Sepunaru et al., 2012).

Numerical Analysis

All the laboratories that tested the different proteins reported, separately, *temperature-independent transport* for each of the three proteins studied here, and the present comparative studies confirm these findings. Such behavior is consistent with tunneling of the electronic carriers as the most efficient transport mechanism over the temperature range that is studied. Naturally, we are well aware of the fact that the separation between the electrodes, imposed by the widths of the protein films, deposited onto the substrates, as measured by AFM (scratching)

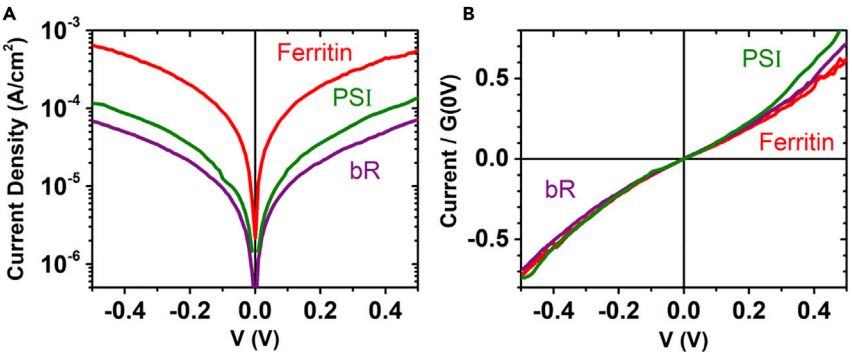

Figure 7. Analysis of Current-Voltage Response of Different Proteins

Comparison of transport characteristics through ^{TS}Au-linker-protein//GaO_x/μch-EGaIn junctions with ferritin (red), bR (purple), and PSI (green) as the protein, showing (A) current density versus voltage on a semi-log scale (from Figure 4, where the errors are also shown); (B) normalized current-voltage, where the equilibrium conductance, G_{eq}, is used as the normalization factor (i.e., the slope at V = 0 equals ~1).

and deduced from ellipsometry, is well beyond the maximal electrode separation of ~4.5 nm to yield measurable tunneling currents across fully conjugated organics (Xie et al., 2015). Reconciling these findings or forwarding different models to explain the temperature independence of solid-state protein junctions is intensively studied these days; we will not enter into this, but refer the reader to recent literature (Bostick et al., 2018; Yuan et al., 2018).

The uncertainty regarding the exact ETp mechanism calls for empirical modeling of the experimental current density (A/cm^2)-voltage (V), *J-V*, curves of the junctions. Such an approach translates the raw *J-V* curves into a few characteristic parameters that can be compared between different junction configurations. Taylor expansion of junction current density as a function of applied bias is one such empirical approach that was very popular in the early days of tunneling research (Brinkman et al., 1970; Simmons, 1963). In practice, expanding up to the third power is sufficient to describe various molecular junctions (Vilan, 2007; Vilan et al., 2013). In addition, the exponential nature of tunneling *J-V* relations allows to factorize the Taylor coefficients in the following manner (Vilan, 2007; Vilan et al., 2013):

$$J = G_{eq} \cdot V \cdot \left[1 + S \cdot \frac{V}{V_0} + \left(\frac{V}{V_0}\right)^2\right] \qquad \text{(Equation 1)}$$

where $G_{eq}(\Omega^{-1}cm^{-2})$, $V_0(V)$, and S(dimensionless) are empirical fitting parameters, called *equilibrium conductance*, *scaling voltage*, and *asymmetry factor*, respectively. The scaled nature of Equation (1) implies that its fitting parameters are orthogonal to each other and their values are independent. This procedure is demonstrated in Figure 7 for one type of junction (μch-EGaIn) for the three different proteins. The semi-log *J-V* presentation for μch-EGaIn (Figure 7A) follows a similar trend to that of Au nanorod (Figure 5) and is dominated by the large variation in transmission probability between the proteins. Within our empirical terminology, it implies variation in G_{eq}, where G_{eq} is simply the slope of *J* versus *V* close to 0 V (Wold and Frisbie, 2001). Dividing each set of *J* values by their corresponding G_{eq} value eliminates the orders of magnitude differences in *J* (without the need to know the value of A_{elec}) and allows comparing the *J-V* traces on a linear scale (Figure 7B). This reveals an almost linear response (Ohmic), where the individual protein identity is expressed at a positive voltage (>0.3 V). Equation (1) was fitted to all measured *J-V* traces (after averaging the traces, for each junction type), and the results are summarized in Table 3 (extended information is given in Table S2 in section B3).

The second parameter V_0 was extracted by fitting the *J-V* curve to Equation (1); to comply with the near-zero expansion nature of Equation (1) the fitting procedure gave larger weight to the low-signal range (normally the fitting range was limited to: |V| < 0.7 V) as further explained in Section B3a of the Supplemental Information. The asymmetry parameter, *S*, was also extracted, but approached zero (ideal, symmetric) in most cases (see Table S2), and therefore will not be discussed further.

In a purist approach, the empirical parameters (G_{eq}, V_0) can be compared across the different junctions directly, as shown on Table 3. As this approach is a bit abstract, we have translated these empirical

Junction			G_{eq} $[mAV^{-1}cm^{-2}]$			Γ_{eff} $[\mu eV]$[a]			ε_0 $[eV]$		
Name	Bottom	Top	bR	PSI	Ferritin	bR	PSI	Ferritin	bR	PSI	Ferritin
n-rod	Au	Au	5,500	7,500	5.2×10^5	130	75	850	0.53	0.20	0.42
LOFO	p^{++}−Si	Au	0.1	0.65	0.83	0.076	0.49	0.34	0.07	0.14	0.14
Hg	p^{++}−Si	Hg	0.03	0.03	0.27	0.036	0.073	0.31	0.07	0.10	0.21
μch	^{TS}Au	EGaIn	0.45	0.15	0.97	0.75	0.45	0.96	0.35	0.27	0.35
Th	^{TS}Au	EGaIn	1.3	0.02	0.001	1.3	0.14	0.023	0.34	0.24	0.24
tip[b]	^{TS}Au	EGaIn	0.0005	0.002	0.001	0.024	0.04	0.018	0.34	0.20	0.19
					0.003			0.049			0.34

Table 3. Summary of Extracted Parameters for Different Junction Configurations (Rows) with Three Different Proteins (Columns)

[a]Γ_{eff} was computed using Eq. 3b from G_{eq} and $\varepsilon_0 = qV_0/2$ and number of molecules, $N = \frac{1E14[nm/cm]^2}{footprint[nm^2]}$, with protein's footprint of 80, 140, and 60 nm^2 for bR, PS-I, and ferritin, respectively. These values are based on protein's diameter and include a factor of 2 for circular surface filling; the bR is further multiplied by 2 to account for surrounding OTG matrix.

[b]tip-EGaIn shows two values for Ferritin: the upper one was measured by UoG (as were the other two proteins) and the lower one by WIS.

observables into specific ETp process parameters. For this purpose, we have chosen the well-accepted single-level Landauer model, where a realistic transmission function is *approximated* by a single, Lorentzian-shaped peak representing only the nearest molecular level (Bâldea, 2012):

$$J = N\frac{2e}{h}\Gamma_g^2\frac{eV}{(\varepsilon_0 + \alpha eV)^2 - (eV/2)^2} \qquad \text{(Equation 2)}$$

Equation 2 is a simplified version of Landauer model under the assumption of $\Gamma \ll |\varepsilon_0|$ and $|V| \leq |\varepsilon_0|$.

Here, ε_0 is the energy of the transmission peak and represents the effective energy difference between the electrode Fermi level and the closest molecular level at zero applied bias; $\Gamma_g^2 = \Gamma_i\Gamma_j$, where Γ_i and Γ_j are the level broadenings by the molecule-electrode couplings at the two (*i*, *j*) electrode/biomolecule interfaces (including organic linker molecules, where applicable); and α is a dimensionless parameter for the deviation from the symmetric partition of the applied voltage between the two contacts, ranging between $-\frac{1}{2} \leq \alpha \leq +\frac{1}{2}$ *and* $\alpha = 0$ for symmetric voltage distribution. Considering that Equation (1) is a modified Taylor expansion, its coefficients are derived from $\frac{d^n J}{d V^n}$ $(n = 1, 2, 3; V = 0)$; this allows a direct translation (or mapping) of the empirical coefficients (Equation (1)) into Landauer-tunneling ones (Equation (2)):

$$\varepsilon_0 \cong \frac{qV_0}{2}\left(assumsing\ S = 0\ and\ \left|\frac{\Gamma_g}{2\varepsilon_0}\right| \ll 1\right) \qquad \text{(Equation 3a)}$$

and

$$\Gamma_g = \frac{\varepsilon_0}{\sqrt{N\frac{G_0}{G_{eq}} - 1}} \qquad \text{(Equation 3b)}$$

G_{eq}, V_0, and S are the parameters extracted from the cubic fit (Equation 1); $\boldsymbol{G_0}$ is the quantum of conductance; and $\boldsymbol{N}$ (molecules/cm^2) is the number of molecules per unit area (as Equation 2 refers to current density; if the fit is to direct current, $\boldsymbol{N}$ would be the absolute number of molecules in the junction). Thus, $\boldsymbol{N}$ essentially reflects the effective electrical contact area ($A_{elec} = \boldsymbol{N} \times$ molecular footprint). As argued earlier, the uncertainty in $\boldsymbol{N}$ (A_{elec}) can be orders of magnitude, which explains why Equation 3b yields only effective values of Γ_g; this restriction is stressed by changing its subscript to effective (Γ_{eff}). Table 3 gives the values of the equilibrium conductance, G_{eq}; its translation into effective coupling energy, Γ_{eff} (using Equation 3b); and the effective energy barrier (Equation 3a).

The most surprising aspect of Table 3 is its low values, both in terms of coupling (Γ_{eff}) and energy barrier ε_0. The energy barrier was in general less than 0.5 eV (which is confirmed by an alternative extraction method of transition voltage spectroscopy (Vilan et al., 2013) (see Section B3b and Table S2). Technically, these low ε_0

values contradict the model of Equation (2), because the model predicts sharp current onsets (conductance resonances) at $|eV| \approx 2\varepsilon_0$, and none are observed, although the voltage range is sufficiently large. This suggests that the potential drop across the junction and its variation with the applied external voltage are different than what is assumed in the simplified model (Equation 2).

The physical intuition suggests that low-lying energy levels (close to the contact's Fermi level) will have strong coupling to the metal's density of states, namely large Γ_{eff} values. Instead, most Γ_{eff} values are extremely low (0.02–1 μeV), way below what is commonly assumed in the field ($\Gamma_{eff} \sim meV$). Note, though, that the oxide-free junction (those with Au nanorods) is much closer to this range ($\Gamma_{eff,\ nanorod} = 0.1 - 0.9\ meV$) and also has a much larger G_{eq} than the other junctions. The larger value of G_{eq} is likely also because a smaller A_{geo} increases the A_{elec}/A_{geo} ratio (Akkerman and de Boer, 2007).

The very small Γ_{eff} values for all junctions except the nanorod ones are likely an artifact because their electric contact area is far smaller than their geometric one. In such a case the number of molecules, N, that participates in the transport is much smaller than the nominal one. Therefore, the apparent values of Γ_{eff}, in Table 3 (and in Table S1), should be considered as the lower limit to Γ_g. Still, considering that $\Gamma_g \propto \frac{1}{\sqrt{N}}$ (Equation 3b) and assuming a realistic Γ_g, of few meV, implies a ratio of A_{elec} over A_{geo} in the order of 10^{-3} to 10^{-6}, supporting our understanding that a very small fraction of the molecules participates in the transport.

Thus, the far higher Γ_{eff} values for nanorod Au-linker-protein//Au junctions can be attributed to the combined effect of a much higher A_{elec}/A_{geo} ratio and better coupling between the protein and electrode energy state (oxide free). A higher A_{elec}/A_{geo} ratio can be understood as follows: the estimation of the nanorod contact area assumes a strip only 10 nm wide; this value is based on geometrical consideration of the distance where a cylinder of 200 nm diameter retracts 1 Å in distance. This width is already at the dimension of a single protein, and therefore in the case of rigid nanorods the effective electrical contacts approaches the nominal one.

In addition to geometrical considerations, chemical and physical details may also influence the coupling. First, nanogold is characterized by strong gold plasmon interactions with the molecular levels (Du et al., 2016; Wu et al., 2016). In addition, this is the only junction in which both contacts are purely metallic without an oxide buffer (GaO_x for EGaIn junctions and SiO_x for Si junctions). Although it can (and has been) argued that these oxides are sufficiently thin so that electrons can tunnel through them efficiently, the oxides do decrease the electronic coupling between the metal that they cover and the proteins and therefore even a thin, poor-quality oxide will reduce Γ_{eff} considerably.

Table 3 also shows very clearly a factor of $\sim 10^2$–10^3 between G_{eq} of μch-EGaIn and tip-EGaIn, an effect that was discussed earlier and is attributed to the much rougher surface, and its effect on A_{geo} and A_{elec}/A_{geo} of tip-EGaIn compared with μch-EGaIn. Obviously, the Γ_{eff} values, derived for tip-EGaIn junctions, are severely underestimated.

Table 3 confirms the conductance trend of **ferritin ≫ PSI > bR** (as is qualitatively observed in Figures 5 and 7) for few types of contacts (nanorod, μch, Hg), but there are many exceptions. We note that reduced contact area cannot explain such trend crossing. We generally ascribe these variations to a combination of factors, including rigidity of the protein layer and differences in the linker chemistry (electrostatic versus covalent binding) for different contact types.

The scaling voltage V_0 and its translation into an effective energy, ε_0, are higher for bR-based junctions than for those with the other two proteins (namely bR's *J-V* response is more linear) with the exception of the ferritin junctions with Si/SiO_x electrodes. Uncertainties (error bar) in V_0 are large, and V_0 values are rather sensitive to the voltage range used to extract them. Interestingly, all three proteins show reasonable to good reproducibility in ε_0 despite a wide distribution of values of Γ_{eff}. We note that G_{eq}, ε_0 and Γ_{eff} also reflect interface effects and as such do not reflect protein-only parameters, explaining why we refer to their values as strictly effective ones. Given the spread of values between different contacts configurations for G_{eq} and Γ_{eff} likely both are dominated by the electrical properties of the contact-protein interface rather than the body of the protein, whereas ε_0 seems robust, indicating that the energy barriers are less affected (the small values for junctions with Si-based contacts can be contributed to electrostatic barriers; cf. Garg et al., 2018). This agrees with the evolving notion of highly efficient charge propagation

along the protein and points to the degree of interfacial electronic coupling as a key player in dictating both the conductance magnitude and its voltage sensitivity.

Conclusion

Comparing charge transport characteristics of (bio)molecular junctions formed with different junction configurations and/or in different laboratories, we find differences of up to three orders of magnitude in geometric area-based (A_{geo} varies in the range of 10^{5}–10^{-3} μm^2) nominal current densities between different junction geometries for the same protein. The variation in current densities is likely due to differences in the actual contacts, i.e., real electrical contact area, compared with geometric one (which often is difficult to define), and in electronic contact-protein coupling. Still, current densities across all different protein-based molecular junctions are temperature independent, which suggests tunneling as the dominant transport process. The efficiency with which the protein is electronically coupled to the electrodes likely varies between contact materials, including their roughness, ways the contact with nominally the same material is made (e.g., nature of GaO_x, cleanliness of Au), the linker used to immobilize the protein, and the orientation of the protein (a polyelectrolyte) on the contact material; all these factors can affect what is termed in electrical engineering, the contact resistance (Fereiro et al., 2018). Overall, our observations lead to the conclusion that for devices with $A_{geo}>10^{2}$ μm^2, the ratios between the "electrical" to measured "geometrical" contact area were relatively uniform, as shown by the small (and in terms of the order of magnitude insignificant) differences between measured current densities for junctions prepared by different fabrication methods in different laboratories. Our conclusions are based on the first set of data from different *molecular bioelectronic* contacting configurations, which also is an unprecedented set of *molecular electronic* data of biomolecular tunnel junctions. In terms of temperature dependence, the results match quite well, and as such, studies that use this tool to learn about transport mechanisms, as well as studies that do not require absolute values for current densities, are transferable from one laboratory to the other. Likely, also length-dependent measurements, wherever possible without subjecting the proteins to tensile or compressive stress, can yield robust results (e.g., of the so-called length decay, β parameter). On the downside, it is hard to compare results using absolute current values as obtained with different junction types and geometries, which calls into question the concept of "conductivity" of a given protein, which often pervades the field. Instead, there is likely a junction conductivity, derived with specific assumptions for the junction conductance, which requires specifying the way the proteins are contacted.

LIMITATIONS OF THE STUDY

Ill-defined micro-structure of the interface between the proteins and the top-contact is a major limitation of solid-state molecular junctions in general. In addition, the shape of the current-voltage response remains close to linear even at relatively high applied voltage, which hinders our ability to identify clear differences in the electronic response of different proteins. Reconciling the efficient long-distance charge transport with lack of temperature activation, is yet challenging.

Resource Availability

Lead Contact

Further information and requests for resources and reagents should be directed to and will be fulfilled by the Lead Contact, Sabyasachi Mukhopadhyay (sabyasachi.m@srmap.edu.in).

Materials Availability

This study did not generate new unique reagents, however proteins used in this study are available from the Lead Contact without restriction.

Data and Code Availability

All data needed to evaluate the conclusions in the paper are present in the paper and/or the Supplemental Information. Additional data related to this paper may be requested from S.M. (sabyasachi.m@srmap.edu.in). Code for NDC analysis and data fitting may be requested from A.V. (ayelet.vilan@weizmann.ac.il).

METHODS

All methods can be found in the accompanying Transparent Methods supplemental file.

SUPPLEMENTAL INFORMATION

Supplemental Information can be found online at https://doi.org/10.1016/j.isci.2020.101099.

ACKNOWLEDGMENTS

S.M. thanks SERB-DST, Govt. of India (award No. ECR/2017/001937) research grants, and the Council for Higher Education (Israel) for a postdoctoral research fellowship at the initial stage of this work. J.F. thanks the Azrieli Foundation for a PD fellowship; C.G. acknowledges a Dean's PD fellowship. At WIS, we thank Dr. Noga Friedman for bR samples, the Minerva Foundation (Munich) and the Israel Science Foundation for partial support. NUS research groups acknowledge the Ministry of Education (MOE) for supporting this research under award No. MOE2015-T2-2-134. Prime Minister's Office, Singapore, under its medium-sized centre program, is also acknowledged for supporting this research. At Groningen the Zernike Institute of Advanced Materials is gratefully acknowledged for financial support. R.M. thanks the Zernike Institute of Advanced Materials; R.C. and V.M. thank the University of Alberta & Alberta Innovates, and R.C. and A.B. thank the National Research Council Canada for financial support.

AUTHOR CONTRIBUTIONS

Conceptualization, A.V., C.A.N., and D.C.; Methodology, S.M., S.K.K., C.G., and A.V.; Investigation, S.M., S.K.K., C.G., J.A.F., A.B., V.M., X.Q., O.E.C.O., X.C., R.R.P., and S.L.; Writing – Original Draft, S.M., S.K.K., and A.V.; Writing –Review & Editing, S.M., S.K.K., A.V., R.C.C., C.G., R.M., C.A.N., and D.C.; Funding Acquisition, S.M., R.C.C., R.M., M.S., C.A.N., and D.C.; Resources, R.C.C., R.M., I.P., M.S., R.R.P., C.A.N., A.V., and D.C.; Supervision, A.B., R.C.C., R.M., I.P., M.S., C.A.N., A.V., and D.C.

DECLARATION OF INTERESTS

The authors declare no competing interests.

Received: December 19, 2019
Revised: March 1, 2020
Accepted: April 20, 2020
Published: May 22, 2020

REFERENCES

Akkerman, H.B., and de Boer, B. (2007). Electrical conduction through single molecules and self-assembled monolayers. J. Phys. Condens. Matter *20*, 013001.

Amdursky, N., Marchak, D., Sepunaru, L., Pecht, I., Sheves, M., and Cahen, D. (2014a). Electronic transport via proteins. Adv. Mater. *26*, 7142–7161.

Amdursky, N., Ferber, D., Bortolotti, C.A., Dolgikh, D.A., Chertkova, R.V., Pecht, I., Sheves, M., and Cahen, D. (2014b). Solid-state electron transport via cytochrome c depends on electronic coupling to electrodes and across the protein. Proc. Natl. Acad. Sci. U S A *111*, 5556–5561.

Bâldea, I. (2012). Ambipolar transition voltage spectroscopy: Analytical results and experimental agreement. Phys. Rev. B *85*, 035442.

Bâldea, I. (2018). Molecular Electronics - an Experimental and Theoretical Approach (Pan Stanford Publishing Pte Ltd.).

Bostick, C.D., Mukhopadhyay, S., Pecht, I., Sheves, M., Cahen, D., and Lederman, D. (2018). Protein bioelectronics: a review of what we do and do not know. Rep. Prog. Phys. *81*, 026601.

Boussaad, S., and Tao, N.J. (1999). Electron transfer and adsorption of myoglobin on self-assembled surfactant films: an electrochemical tapping-mode AFM study. J. Am. Chem. Soc. *121*, 4510–4515.

Brinkman, W.F., Dynes, R.C., and Rowell, J.M. (1970). Tunneling conductance of asymmetrical barriers. J. Appl. Phys. *41*, 1915–1921.

Cademartiri, L., Thuo, M.M., Nijhuis, C.A., Reus, W.F., Tricard, S., Barber, J.R., Sodhi, R.N.S., Brodersen, P., Kim, C., Chiechi, R.C., et al. (2012). Electrical resistance of AgTS–S(CH2)n−1CH3// Ga2O3/EGaIn tunneling junctions. J. Phys. Chem. C *116*, 10848–10860.

Castañeda Ocampo, O.E., Gordiichuk, P., Catarci, S., Gautier, D.A., Herrmann, A., and Chiechi, R.C. (2015). Mechanism of orientation-dependent asymmetric charge transport in tunneling junctions comprising photosystem I. J. Am. Chem. Soc. *137*, 8419–8427.

Chen, X., Hu, H., Trasobares, J., and Nijhuis, C.A. (2019). Rectification ratio and tunneling decay coefficient depend on the contact geometry revealed by in situ imaging of the formation of EGaIn junctions. ACS Appl. Mater. Interfaces *11*, 21018–21029.

Chiechi, R.C., Weiss, E.A., Dickey, M.D., and Whitesides, G.M. (2008). Eutectic gallium–indium (EGaIn): a moldable liquid metal for electrical characterization of self-assembled monolayers. Angew. Chem. Int. Ed. *47*, 142–144.

Dickey, M.D. (2017). Stretchable and soft electronics using liquid metals. Adv. Mater. *29*, 1606425.

Du, W., Wang, T., Chu, H.-S., Wu, L., Liu, R., Sun, S., Phua, W.K., Wang, L., Tomczak, N., and Nijhuis, C.A. (2016). On-chip molecular electronic plasmon sources based on self-assembled monolayer tunnel junctions. Nat. Photon. *10*, 274.

Fereiro, J.A., Porat, G., Bendikov, T., Pecht, I., Sheves, M., and Cahen, D. (2018). Protein electronics: chemical modulation of contacts control energy level alignment in gold-azurin-gold junctions. J. Am. Chem. Soc. *140*, 13317–13326.

Gaigalas, A.K., and Niaura, G. (1997). Measurement of electron transfer rates between

adsorbed azurin and a gold electrode modified with a hexanethiol layer. J. Colloid Interface Sci. *193*, 60–70.

Garg, K., Raichlin, S., Bendikov, T., Pecht, I., Sheves, M., and Cahen, D. (2018). Interface electrostatics dictates the electron transport via bioelectronic junctions. ACS Appl. Mater. Interfaces *10*, 41599–41607.

Guo, C., Yu, X., Refaely-Abramson, S., Sepunaru, L., Bendikov, T., Pecht, I., Kronik, L., Vilan, A., Sheves, M., and Cahen, D. (2016). Tuning electronic transport via hepta-alanine peptides junction by tryptophan doping. Proc. Natl. Acad. Sci. U S A *113*, 10785–10790.

Haick, H., and Cahen, D. (2008). Contacting organic molecules by soft methods: towards molecule-based electronic devices. Acc. Chem. Res. *41*, 359–366.

Holm, R. n.d., Electric Contacts: Theory and Application (Springer-Verlag Berlin Heidelberg).

Jiang, L., Sangeeth, C.S.S., Wan, A., Vilan, A., and Nijhuis, C.A. (2015). Defect scaling with contact area in EGaIn-based junctions: impact on quality, joule heating, and apparent injection current. J. Phys. Chem. C *119*, 960–969.

Jin, Y., Friedman, N., Sheves, M., He, T., and Cahen, D. (2006). Bacteriorhodopsin (bR) as an electronic conduction medium: current transport through bR-containing monolayers. Proc. Natl. Acad. Sci. U S A *103*, 8601–8606.

Jin, Y., Honig, T., Ron, I., Friedman, N., Sheves, M., and Cahen, D. (2008). Bacteriorhodopsin as an electronic conduction medium for biomolecular electronics. Chem. Soc. Rev. *37*, 2422–2432.

Kumar, K.S., Pasula, R.R., Lim, S., and Nijhuis, C.A. (2016). Long-range tunneling processes across ferritin-based junctions. Adv. Mater. *28*, 1824–1830.

Kumar, K.S., Troadec, C., Vilan, A., and Nijhuis, C.A. (2019). Ultra-smooth photoresist-free micropore-based EGaIn molecular junctions: fabrication and how roughness determines voltage response. Adv. Funct. Mater. *29*, 1904452.

Lovrinčić, R., Kraynis, O., Har-Lavan, R., Haj-Yahya, A., Li, W., Vilan, A., and Cahen, D. (2013). A new route to nondestructive top-contacts for molecular electronics on Si: Pb evaporated on organic monolayers. J. Phys. Chem. Lett. *4*, 426–430.

McCreery, R.L., Yan, H., and Bergren, A.J. (2013). A critical perspective on molecular electronic junctions: there is plenty of room in the middle. Phys. Chem. Chem. Phys. *15*, 1065–1081.

Moulton, S.E., Barisci, J.N., Bath, A., Stella, R., and Wallace, G.G. (2003). Investigation of protein adsorption and electrochemical behavior at a gold electrode. J. Colloid Interface Sci. *261*, 312–319.

Mukhopadhyay, S., Dutta, S., Pecht, I., Sheves, M., and Cahen, D. (2015). Conjugated cofactor enables efficient temperature-independent electronic transport across ~6 nm long halorhodopsin. J. Am. Chem. Soc. *137*, 11226–11229.

Nijhuis, C.A., Reus, W.F., Barber, J.R., Dickey, M.D., and Whitesides, G.M. (2010a). Charge transport and rectification in arrays of SAM-based tunneling junctions. Nano Lett. *10*, 3611–3619.

Nijhuis, C.A., Reus, W.F., and Whitesides, G.M. (2010b). Mechanism of rectification in tunneling junctions based on molecules with asymmetric potential drops. J. Am. Chem. Soc. *132*, 18386–18401.

Nijhuis, C.A., Reus, W.F., Barber, J.R., and Whitesides, G.M. (2012). Comparison of SAM-based junctions with Ga2O3/EGaIn top electrodes to other large-area tunneling junctions. J. Phys. Chem. C *116*, 14139–14150.

Ratner, M. (2013). A brief history of molecular electronics. Nat. Nano *8*, 378–381.

Regan, M.J., Tostmann, H., Pershan, P.S., Magnussen, O.M., DiMasi, E., Ocko, B.M., and Deutsch, M. (1997). X-ray study of the oxidation of liquid-gallium surfaces. Phys. Rev. B *55*, 10786–10790.

Reus, W.F., Nijhuis, C.A., Barber, J.R., Thuo, M.M., Tricard, S., and Whitesides, G.M. (2012). Statistical tools for analyzing measurements of charge transport. J. Phys. Chem. C *116*, 6714–6733.

Ron, I., Pecht, I., Sheves, M., and Cahen, D. (2010). Proteins as solid-state electronic conductors. Acc. Chem. Res. *43*, 945–953.

Rothemund, P., Morris Bowers, C., Suo, Z., and Whitesides, G.M. (2018). Influence of the contact area on the current density across molecular tunneling junctions measured with EGaIn top-electrodes. Chem. Mater. *30*, 129–137.

Salomon, A., Cahen, D., Lindsay, S., Tomfohr, J., Engelkes, V.B., and Frisbie, C.D. (2003). Comparison of electronic transport measurements on organic molecules. Adv. Mater. *15*, 1881–1890.

Sana, B., Johnson, E., Sheah, K., Pho, C.L., and Lim, S. (2010). Biointerphases *5*, 48, https://doi.org/10.1116/1.3483216.

Sangeeth, C.S.S., Wan, A., and Nijhuis, C.A. (2014). Equivalent circuits of a self-assembled monolayer-based tunnel junction determined by impedance spectroscopy. J. Am. Chem. Soc. *136*, 11134–11144.

Sangeeth, C.S.S., Demissie, A.T., Yuan, L., Wang, T., Frisbie, C.D., and Nijhuis, C.A. (2016). Comparison of DC and AC transport in 1.5–7.5 nm oligophenylene imine molecular wires across two junction platforms: eutectic Ga–In versus conducting probe atomic force microscope junctions. J. Am. Chem. Soc. *138*, 7305–7314.

Sayed, S.Y., Fereiro, J.A., Yan, H., McCreery, R.L., and Bergren, A.J. (2012). Charge transport in molecular electronic junctions: Compression of the molecular tunnel barrier in the strong coupling regime. Proc. Natl. Acad. Sci. U S A *109*, 11498–11503.

Schnyder, B., Kotz, R., Alliata, D., and Facci, P. (2002). Comparison of the self-chemisorption of azurin on gold and on functionalized oxide surfaces. Surf. Interf. Anal. *34*, 40–44.

Seitz, O., Böcking, T., Salomon, A., Gooding, J.J., and Cahen, D. (2006). Importance of monolayer quality for interpreting current transport through organic molecules: alkyls on oxide-free Si. Langmuir *22*, 6915–6922.

Sepunaru, L., Friedman, N., Pecht, I., Sheves, M., and Cahen, D. (2012). Temperature-dependent solid-state electron transport through bacteriorhodopsin: experimental evidence for multiple transport paths through proteins. J. Am. Chem. Soc. *134*, 4169–4176.

Simeone, F.C., Yoon, H.J., Thuo, M.M., Barber, J.R., Smith, B., and Whitesides, G.M. (2013). Defining the value of injection current and effective electrical contact area for EGaIn-based molecular tunneling junctions. J. Am. Chem. Soc. *135*, 18131–18144.

Simmons, J.G. (1963). Low-voltage current-voltage relationship of tunnel junctions. J. Appl. Phys. *34*, 238–239.

Singhal, G.S., Renger, G., Sopory, S.K., Irrgang, K.D., and Govindjee, R. (1999). Concepts in Photobiology: Photosynthesis and Photomorphogenesis (Springer Netherlands).

Tao, N.J. (2006). Electron transport in molecular junctions. Nat. Nano *1*, 173–181.

Timsit, R.S. (1982). The true area of contact at a liquid metal-solid interface. Appl. Phys. Lett. *40*, 379–381.

Vilan, A. (2007). Analyzing molecular current-voltage characteristics with the simmons tunneling model: scaling and linearization. J. Phys. Chem. C *111*, 4431–4444.

Vilan, A. (2017). Revealing tunnelling details by normalized differential conductance analysis of transport across molecular junctions. Phys. Chem. Chem. Phys. *19*, 27166–27172.

Vilan, A., and Cahen, D. (2002). Soft contact deposition onto molecularly modified GaAs. thin metal film flotation: principles and electrical effects. Adv. Funct. Mater. *12*, 795–807.

Vilan, A., Cahen, D., and Kraisler, E. (2013). Rethinking transition voltage spectroscopy within a generic taylor expansion view. ACS Nano *7*, 695–706.

Vilan, A., Aswal, D., and Cahen, D. (2017). Large-area, ensemble molecular electronics: motivation and challenges. Chem. Rev. *117*, 4248–4286.

Waleed Shinwari, M., Jamal Deen, M., Starikov, E.B., and Cuniberti, G. (2010). Electrical conductance in biological molecules. Adv. Funct. Mater. *20*, 1865–1883.

Wan, A., Jiang, L., Sangeeth, C.S.S., and Nijhuis, C.A. (2014). Reversible soft top-contacts to yield molecular junctions with precise and reproducible electrical characteristics. Adv. Funct. Mater. *24*, 4442–4456.

Wold, D.J., and Frisbie, C.D. (2001). Fabrication and characterization of metal−molecule−metal junctions by conducting probe atomic force microscopy. J. Am. Chem. Soc. *123*, 5549–5556.

Wu, L., Tan, S.F., Bosman, M., Yang, J.K.W., Nijhuis, C.A., and Bai, P. (2016). Charge

transfer plasmon resonances across silver–molecule–silver junctions: estimating the terahertz conductance of molecules at near-infrared frequencies. RSC Adv. *6*, 70884–70894.

Xie, Z., Bâldea, I., Smith, C.E., Wu, Y., and Frisbie, C.D. (2015). Experimental and theoretical analysis of nanotransport in oligophenylene dithiol junctions as a function of molecular length and contact work function. ACS Nano *9*, 8022–8036.

Yan, H., Bergren, A.J., and McCreery, R.L. (2011). All-carbon molecular tunnel junctions. J. Am. Chem. Soc. *133*, 19168–19177.

Yu, X., Lovrinčić, R., Kraynis, O., Man, G., Ely, T., Zohar, A., Toledano, T., Cahen, D., and Vilan, A. (2014). Fabrication of reproducible, integration-compatible hybrid molecular/si electronics. Small *10*, 5151–5160.

Yu, X., Lovrincic, R., Sepunaru, L., Li, W., Vilan, A., Pecht, I., Sheves, M., and Cahen, D. (2015). Insights into solid-state electron transport through proteins from inelastic tunneling spectroscopy: the case of azurin. ACS Nano *9*, 9955–9963.

Yuan, L., Wang, L., Garrigues, A.R., Jiang, L., Annadata, H.V., Anguera Antonana, M., Barco, E., and Nijhuis, C.A. (2018). Transition from direct to inverted charge transport Marcus regions in molecular junctions via molecular orbital gating. Nat. Nanotechnol. *13*, 322–329.

iScience, Volume *23*

Supplemental Information

Solid-State Protein Junctions: Cross-Laboratory Study Shows Preservation of Mechanism at Varying Electronic Coupling

Sabyasachi Mukhopadhyay, Senthil Kumar Karuppannan, Cunlan Guo, Jerry A. Fereiro, Adam Bergren, Vineetha Mukundan, Xinkai Qiu, Olga E. Castañeda Ocampo, Xiaoping Chen, Ryan C. Chiechi, Richard McCreery, Israel Pecht, Mordechai Sheves, Rupali Reddy Pasula, Sierin Lim, Christian A. Nijhuis, Ayelet Vilan, and David Cahen

Supplemental Information

Contents

Transparent Methods

Section A.

1. Materials

1a. Protein Preparation Methodology

(i) Ferritin

The ferritins used here originate from the hyper-thermophilic archaeon *Archaeoglobus fulgidus* (PDB - 1S3Q), which has high thermal stability (up to 80°C). Ferritins convert aqueous Fe^{2+} into insoluble Fe^{3+} in the form of ferrihydrite nanoparticles. The ferritin iron composites were prepared via previously reported procedures.(Kommareddy et al., 2010) Expression and purification of A. fulgidus ferritin (AfFtn) was performed as described elsewhere.(Kommareddy et al., 2010) Here ferritin were isolated from the E.coli BL21(DE3)C+RIL cells (Stratagene, Santa Clara, CA), protein quantification was performed using the BCA assay kit (Thermo Fisher Scientific Inc, Rockford, USA).

Iron loading in Ferritin: Iron loading into ferritin was carried out, by incubating apo-Ferritin with freshly prepared ferrous sulfate solution in 0.1% HCl for 1 hour at room temperature followed by overnight incubation at 4°C. Different iron loadings were achieved by adding required moles of iron sulfate solution to the dimeric ferritin solution (1 µM ferritin = 500 µg/ml ferritin). Amicon centrifugal filters (100 kDa MWCO; Millipore, Billerica, MA) were used to remove the unbound iron by buffer exchange. Protein quantification was performed using the BCA assay kit (Thermo Fisher Scientific Inc, Rockford, USA).(Kommareddy et al., 2010)

(ii) OTG-bacteriorhodopsin

Well established vesicle fusion tactics been utilized to reconstitute bR (PDB - 1FBB) in lipid bilayers on a solid, electrically conducting support. A detailed description of the preparation of OTG-bacteriorhodopsin is available in reference(Jin et al., 2006, 2008)

(iii) PSI

PSI protein was isolated and cleaned from the complexes from thermophilic unicellular cyanobacterium *Thermosynechococcus elongates* BP-1 (PDB - 6HUM) which evolutionally formed a trimer structure for improved light absorption efficiency and stability at harsh conditions. The monomer of PSI has a polar stroma and lumen and an apolar backbone. Its size is approximately 13 × 8 × 9 nm and contains 96 light sensitive Chlorophyll a (Chla) molecules that are densely packed in the protein scaffold to harvest light. A detailed description of the preparation is available in reference(Castañeda Ocampo et al., 2015)

1b. Protein storage

Ferritin and PSI were kept till use at -80 °C; protein quality was examined through optical absorptions, CD and other measurements as required. OTG-bR in 0.01M phosphate buffer solution was distributed at 25° C, as this protein is stable at 25 – 30 °C for ~ 4 months. It is stable thermally until 70 °C.

1c. Substrate preparation for Protein SAM deposition

(a) Preparation of Template-stripped Au substrate (^{TS}Au)

A 100 nm thin film of gold (Au) is directly evaporated on Si/SiO_2, freshly cleaned, using Piranha treatment, at a very slow rate of 0.1-0.2 Å/s using an E-beam evaporator. A cleaned glass slide is glued onto the Au layer with UV curable glue (NOA61). After curing the glue with UV exposure for 2 hours, the Au layer was stripped from the Si/SiO_2 substrate, ready for its use.

(b) Preparation of Silicon substrate (Si/SiO_x)

The <100> surface of a highly doped p-type Si wafer (Virginia Semiconductor Inc.; <0.001 Ω cm) was first pre-cleaned by sequential acetone-isopropyl alcohol (1:1) and ethyl acetate/ethanol (5 min in each) bath sonications, for which the wafer was placed in a glass test tube. Next the wafer was cleaned by 30 min piranha treatment (7/3 v/v of H_2SO_4/H_2O_2) on a hot plate (~ 80°C). The wafer

was then thoroughly rinsed with Milli-Q (18 MΩ) water, and dipped in 2% HF solution for 1 minute to remove the silicon oxide surface, leaving a Si-H surface). A thin oxide layer (9 - 10 Å) was grown controllably on the etched Si wafer in a fresh piranha solution for 20 - 30 sec, followed immediately by thorough rinsing by Milli-Q water and drying under a nitrogen stream. A self-assembled monolayer of 3-AminoPropyl TriMethoxySilane (3-APTMS, NH2-terminated linker, 97%, Sigma-Aldrich) was prepared by immersing the resulting SiO_x-covered Si wafer overnight in a 16% (volume) 3-APTMS in methanol solution, followed by 3 min of bath sonication in methanol and cleaning with Milli-Q water, yielding a monolayer thickness of ~ 5 – 6 Å.

2. Characterization

2a. Reference sample characterization

Standard molecule-based tunneling junctions were fabricated with a carbon-NAB//e-C//Au (NAB - 4-[2-(4-nitrophenyl) diazenyl]-phenyl groups) configuration. Before the carbon (10 nm) and gold (15 nm) evaporation as permanent top contact, NAB monolayers were characterized by tapping mode topography image using a Nanoscope III, a multimode instrument (Digital Instruments, Santa Barbara, CA), with etched silicon probes (RTESP) with resonant frequencies of ~ 300 kHz (Veeco, Sunnyvale, CA). RMS roughness of the film was found to be ~ 0.5 nm scale and no extra layer formation was observed in the AFM image.

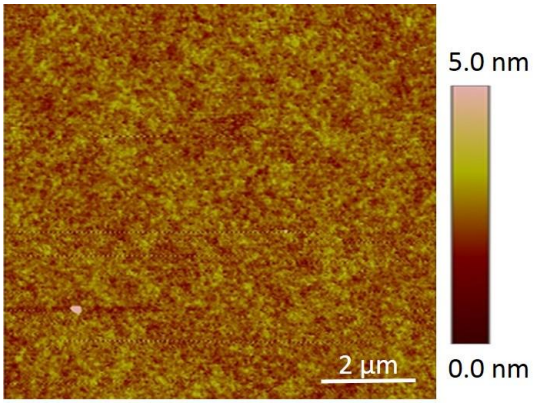

Figure S1. Related to Figure 3 - 'Standard' Molecular Junction: Tapping mode atomic force microscope image of NAB monolayer on carbon electrode substrate.

2b. Protein Monolayer Preparation and Characterization

In our previous studies we observed that roughness of the protein monolayers and a poor-quality SAM (coverage of protein Self-Assembled Monolayer on ^{TS}Au and p^{++}-Si/SiO_x) do effect the junction current density (when normalized with A_{geo}) to a certain extent (Castañeda Ocampo et al., 2015). Thus, before electrical measurements, we assured the *quality* of all protein SAMs developed on ^{TS}Au and p^{++}-Si/SiO_x using semi-contact/tapping mode AFM topography imaging.

At NUS, a Bruker (Bruker-Nano, Santa Barbara, CA, USA) Dimension Fastscan with FASTSCAAN-A, resonance frequency 1.4 MHz, force constant – 18 N/m was used to image 1μm × 1μm square area. Roughness and coverage of protein SAMs were obtained using nanoscope analysis (version 1.4) software.

At WIS, a Solver P47 (NT-MDT, Zelenograd, Russia) and Multimode/Nanoscope-V Scanning Probe Microscopy system were used in combination with Pt-coated Si probes (80 kHz, 2.8 N/m from Mikromasch). Topography and phase images were obtained simultaneously at a scan

rate of 1 Hz. Roughness and coverages protein SAMs was obtained using Gwyddion (version 2) software.

At UOG, a Bruker AFM Multimode MMAFM-2 with Au-coated silicon nitride tip (NPG-10, Bruker; tip A, resonant frequency 65 kHz, spring constant 0.35 N/m) was utilized to image protein SAMs and analyzed with the nanoscope software.

(i) Ferritin monolayer on ^{TS}Au

(a) Freshly prepared *self-assembled monolayers* (SAM) of 6-mercapto hexanoic acid (MHA) or 3-mercaptopropionic acid (MPA) on template-stripped gold (^{TS}Au) substrate was used to immobilize ferritin. Ferritin was covalently bound to the MHA or MPA linker layer with carbodiimide crosslinker chemistry (EDC/NHS reaction). The monolayer-modified ^{TS}Au substrates were rinsed by ethanol and dried with N_2 gas. Subsequently, the functionalized substrate was immersed in 1-ethyl-3-(-3-imethylaminopropyl) carbodiimide hydrochloride (EDC; 50 mg/mL) for 2 hour to activate the surface carboxylic group on the ^{TS}Au substrate. The surface-activated sample was immersed overnight in humid environment, in a 0.01M phosphate buffer solution containing ferritin (1 mg/mL). Finally, the sample was indirectly rinsed in deionized water to remove non-specifically bound ferritin from the monolayer, and blown dry with N_2 gas. Ferritin monolayers on freshly template-stripped ^{TS}Au substrates were examined with ellipsometry and tapping mode AFM imaging in the different laboratories.

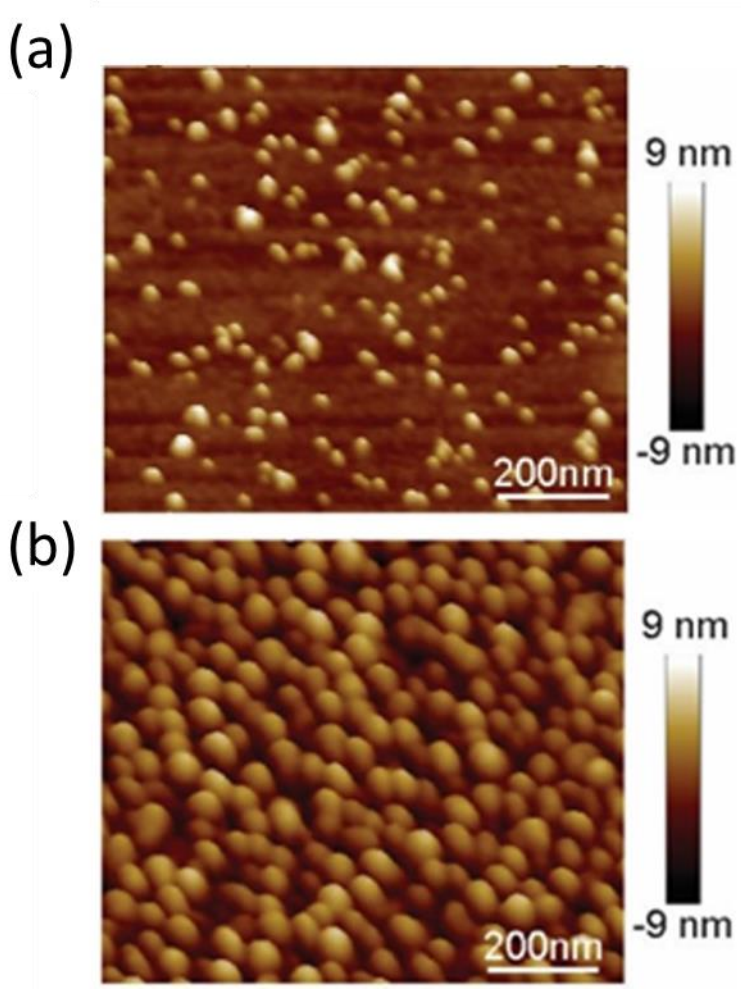

Figure S2. Related to Table 2: AFM image of ferritin monolayer (^{TS}Au//MHA-EDC) as used for RT and temperature-dependent electrical measurements. (a) Incubation with low concentration ferritin

solution for individual size measurements and (b) incubation with optimized ferritin solution for packed SAM preparation towards electrical measurements.

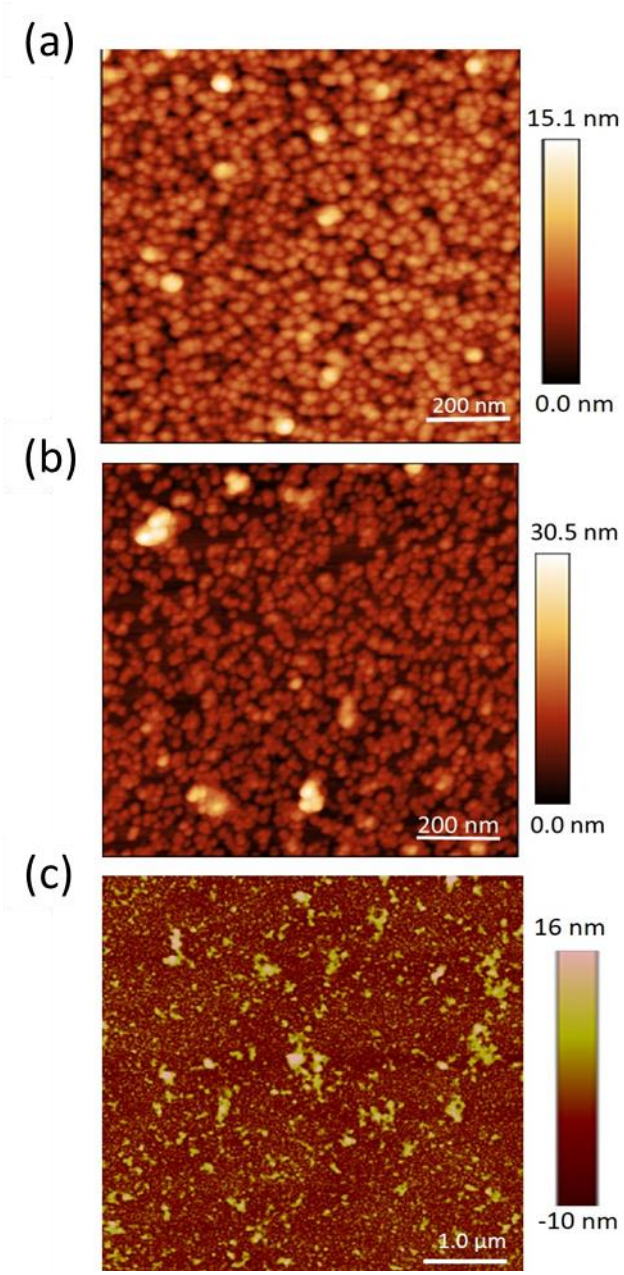

Figure S3. Related to Table 2: (a) Tapping mode AFM image of ferritin monolayer on MPA-EDC - modified ^{TS}Au after overnight incubation; (b) and (c): AFM images of ferritin protein monolayer (Au^{TS}/MHA-EDC).

(b) APTMS-treated, freshly cleaned Si (p^{++})/SiO_x was immersed in a Ferritin solution (1 mg/ml) overnight at 4°C. After immersion substrates were rinsed in buffer and Milli-Q water and dried under a slow stream of N_2 gas. The thickness of the protein monolayer on the substrate was examined using ellipsometry measurements. The ferritin monolayers on APTMS-treated silicon substrates were characterized by tapping mode AFM topography. Protein layer thickness of ~ 6 - 7 nm was obtained from ellipsometry and 6 – 8 nm with nano-scratching mode AFM.

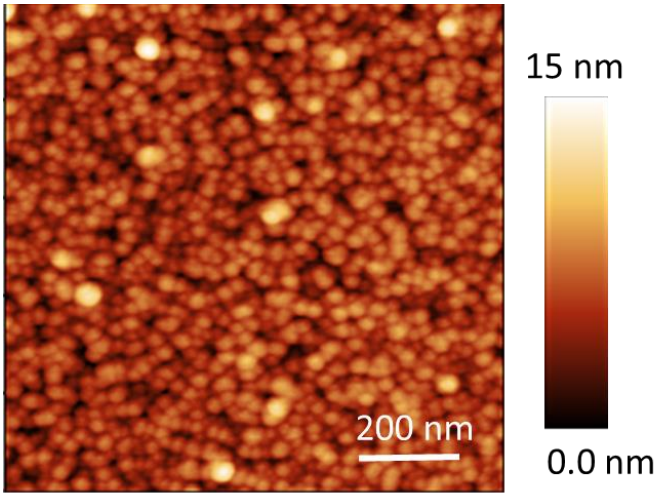

Figure S4. Related to Table 2: Tapping mode AFM image of ferritin monolayer on Si/SiO_x surface

(ii) OTG-bacteriorhodopsin

(a) A template-stripped (^{TS}Au) substrate was immersed into a 3 mM solution of Cysteamine or 6-amino-1-hexanethiol solution in 20 mL water for 2 hours. After functionalization, the ^{TS}Au substrate was washed with water and dried with N_2. The functionalized ^{TS}Au was incubated in the OTG-bR solution (0.2 OD) for 30 - 60 min, and then transferred to deionized water for another 2.5 - 3 hr. Finally samples were indirectly washed in deionized water, and dried with N_2. The OTG-bR film on the linker molecule-functionalized stripped ^{TS}Au substrate was examined with ellipsometry and tapping mode AFM imaging.

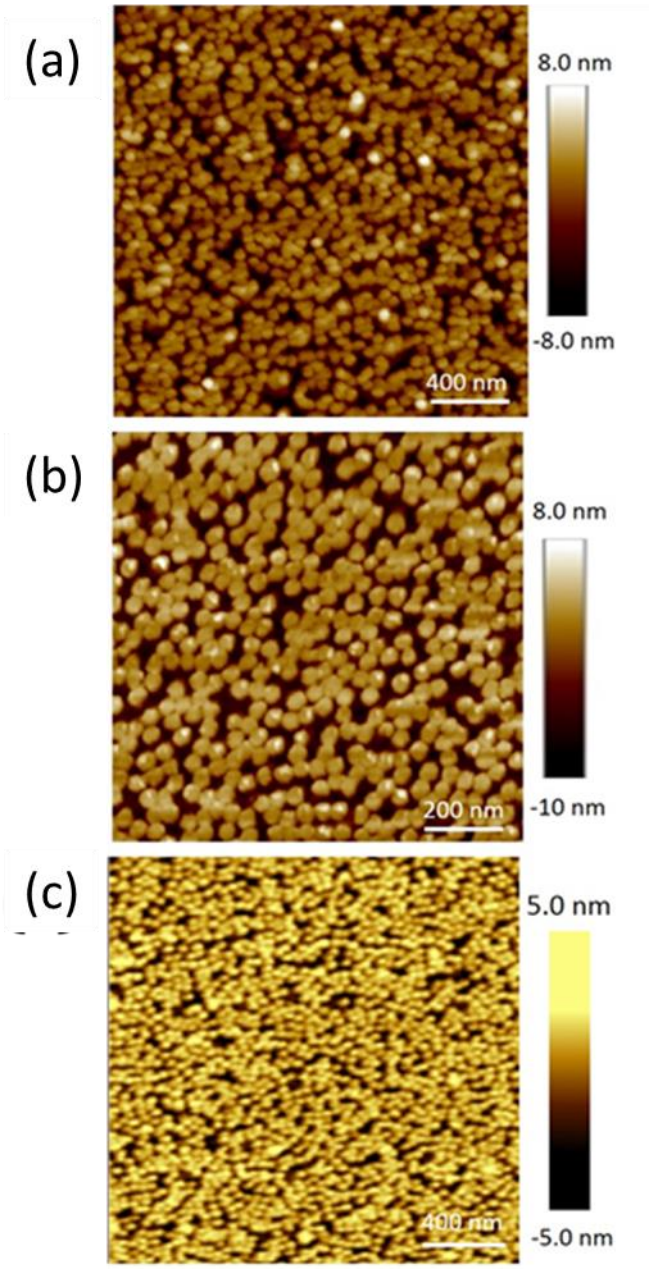

Figure S5. Related to Table 2: AFM image of bR adsorbed on ^{TS}Au using two different types of linker molecules (a) 6-amino-1-hexanethiol and (b) – (c) cysteamine.

(b) Monolayers of OTG-bR protein were prepared via self-assembly of protein vesicles on APTMS-treated Si-SiO_x substrates with 30 min incubation of the substrate in the protein solution (0.2 OD), followed by water incubation for 2.5 – 3 hours at room temperature. OTG-bR layers on silicon were characterized by tapping mode AFM. The average thickness was 7 nm from ellipsometry and from tapping mode AFM (as examined for surface exposed to diluted film formation conditions using the nano-scratching method).

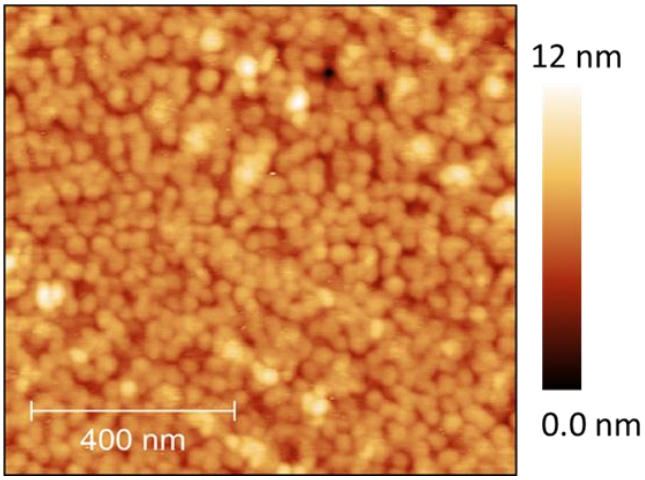

Figure S6. Related to Table 2: Tapping mode AFM image of OTG-bR on Silicon substrate.

(iii) PSI

(a) A template-stripped ^{TS}Au substrate was immersed into a 1 mM solution of 3-mercaptopropionic acid, MPA or 1 mM 2- mercaptoethanol, 2ME solution in 20 mL water for two hours. After functionalization, the ^{TS}Au substrates were washed with water and dried with N_2. MPA or 2ME-functionalized ^{TS}Au was incubated with PSI solution (1:1 ratio of PS-I and buffer (20 mM HEPES (pH 7.5); 10 mM $MgCl_2$; 10 mM $CaCl_2$; 500 mM Mannitol with 0.05% DDM (n-Dodecyl-β-D-Maltoside) for 2 hr, in the dark, followed by washing with water, and dried with N_2. Samples were stored in a cool (<23 - 5 °C) and dark place (dry box, RH < 15%) before electrical measurements. PSI monolayers on linker molecule-functionalized template-stripped ^{TS}Au substrates were examined with ellipsometry and tapping mode AFM imaging at all three laboratories.

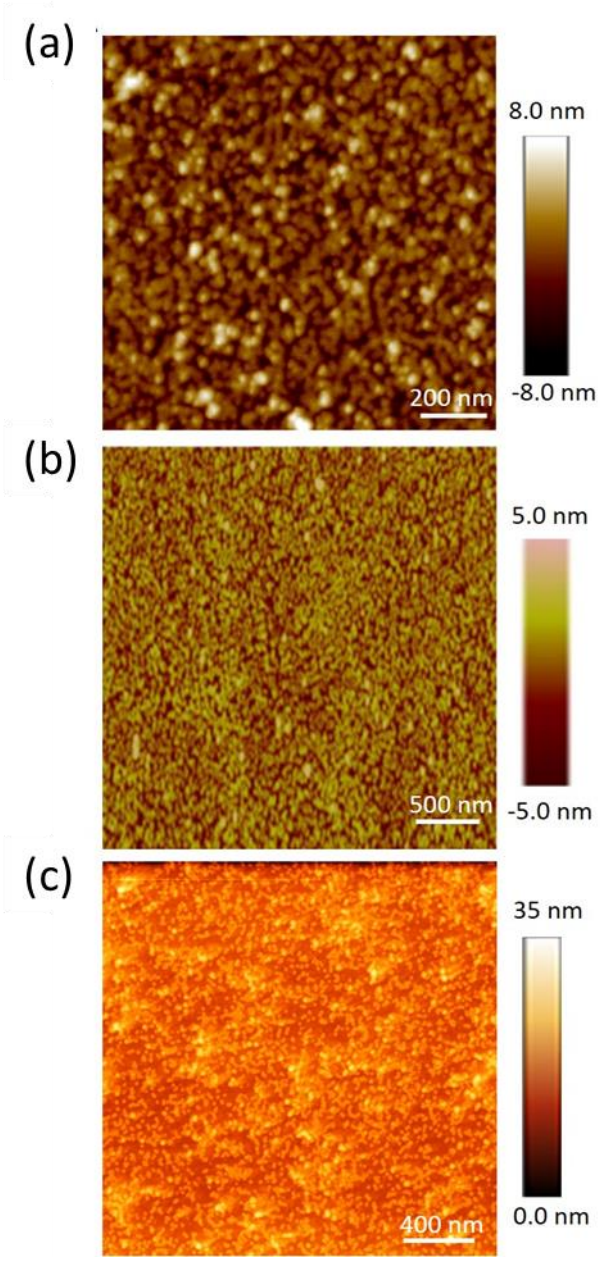

Figure S7. Related to Table 2: Topography image (AFM) of PSI adsorbed on ^{TS}Au (a) 3-mercaptopropionic acid (b and c) 2- mercaptoethanol as linker molecules at different laboratories, (adapted from Reference(Castañeda Ocampo et al., 2015) with permission from reference)

(b) PS-I monolayers were prepared by dropping a PS-I solution on APTMS-modified Si-SiO_x substrates and incubating overnight at 4° C. Finally, samples were indirectly cleaned with water and dried with N_2 flow. Samples were instantly used for LOFO deposition and electrical measurements were carried out after vacuum drying for 4 - 8 hours. The PSI monolayers on silicon were also examined with ellipsometry and tapping mode AFM imaging. From ellipsometry we calculate a 7.5 nm height and Nano-scratching gave 7.5 – 8 nm thickness.

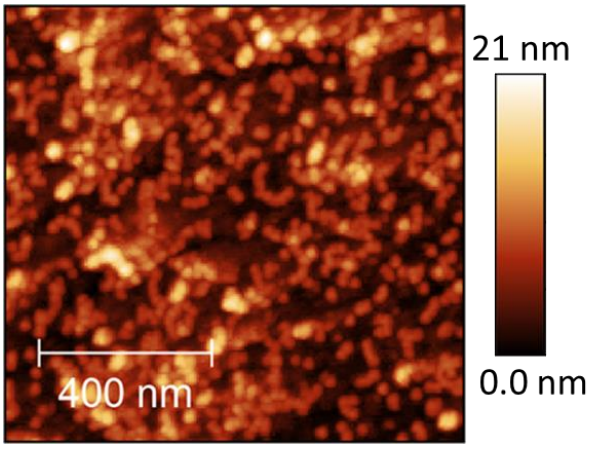

Figure S8. Related to Table 2: Tapping mode AFM images of PSI monolayer on with overnight incubation with APTMS-treated Si-SiO_x substrate.

3. Room Temperature Electrical Measurements

3a. Electrical measurement of standard molecular junction

Current –voltage of the carbon/NAB/C-Au, a permanent contact molecular junction of area – 1.25 $\times$ 10^5 μm^2, were measured at all the contributing laboratories, starting with Edmonton (UoA, Canada); followed by WIS, Israel; NUS, Singapore and UoG, the Netherlands. At UoA and NUS, reference NAB junctions were examined with both 2-probe and 4-probe configuration (to eliminate external contact resistances).

Within the Landauer tunneling transport formulism, the measured current densities reflect the quantum mechanical electron transport function $\Gamma_{Junction} = \Gamma_{Eletrode\ 1} \times \Gamma_{molecule} \times \Gamma_{Electrode\ 2}$, which includes the contributions of (internal) interface contact resistances. Differences between 2- and 4-probe measurements were minit and, because not all labs had 4-probe measurement capabilities, we focus on the results of the 2-probe measurements, also because only 2-probe measurements were feasible on the protein junctions. (Figure 3 in main text).

As a further check on one of the contacting schemes, we also measured *non-encapsulated* carbon/NAB samples, with cone-shaped EGaIn as the top electrode. Current densities were about four orders of magnitude lower than those with the evaporated carbon-gold top-contacts (Figure – S9). This very large difference could stem from (i) what might be the smaller ratio between effective and geometric contact area with this type of EGaIn contact(Simeone et al., 2013) than with the other contacts,(Salomon et al., 2003) (ii) contamination of the exposed NAB surface with time during shipping, stressing the importance of effective encapsulation of the complete NAB devices. An additional factor for the large difference between the permanent, encapsulated evaporated Au and the temporary EGaIn cone contacts may be contact quality/ coupling efficiency (for any contact material and method). We note this because Au/bR/Au nanorod junctions yield (at 0.5 V bias) 3.5 orders of magniture higher current density (using the area values given in the text) than Au/bR/EGaIn cone ones and both are not encapsulated.

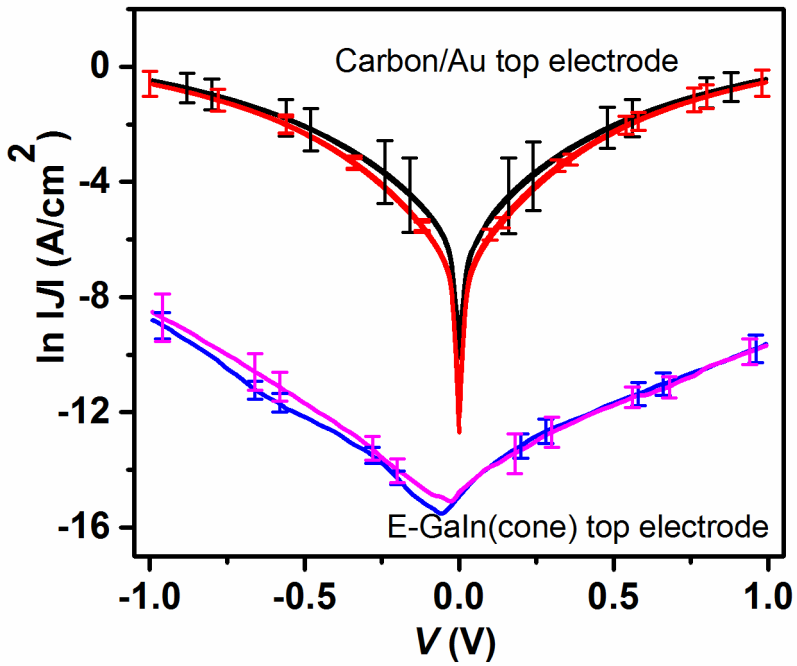

Figure S9. Related to Figure 3 - Calibration by 'standard' molecular junction: Comparison between C-NAB//e-C//Au and C-NAB//GaO_x/tip-EGaIn devices with their electrical measurement. Error bars represents statistical variations in current densities over ~ 70 *I-V* traces for 10 different devices from each fabricated batch. were was fabricated at UoA in two different batches to check the consistency of the experimental results (Red – Blue: Batch I and Black-Violet: Batch II)

In our comparison measurements, biomolecule - based junctions were individually fabricated at different laboratories following the protocols, to avoid contamination or degradation of proteins in the devices. We stress that if one encapsulates the junctions effectively, then biomolecule-based junction devices may well be stable enough to be distributed to different laboratories for electrical characterizations, as is now the case with the NAB junctions, even though the protein layer and its contacts will remain less robust than a molecular layer, such as NAB, and contacts to it.

3b. Electrical measurement of bioelectronic (Protein) junctions

In each laboratory, *I-V* measurements were carried out with devices fabricated with several batches of protein monolayers. Each device was tested by taking 5- 20 repetitive *I-V* scans (each starts at **0** V → **+1** V → **–1** V → **0** V) to examine the consistency of the current amplitude from each junction. In general, the error bars in the plots are obtained by taking the arithmetic mean of the *sets of I-V curves*, while for the numerical analysis *individual I-V plots* were analyzed and the errors are based on the spread of the results that we obtained.

(I) E-GaIn cone shaped contact (with ^{TS}Au substrate)

Electrical measurements (at WIS) were performed in a custom-built Faraday cage using a Keithley 6430 Sub-Femtoamp Remote Source Meter SMU. The device was held in place with a spring-loaded gold tip that was isolated from ground. Bias was applied to a syringe filled with E-GaIn. Data were obtained from an average of points by sweeping the potential from −1.0 to 1.0 V at a rate of 0.2 V/s. A statistical deviation over around ~ 50 junctions were represented as error bars.
At UoG and NUS electrical measurements (Current vs. voltage were carried out in ambient conditions with cone-shaped E-GaIn tip junctions. Average geometric area of each junction as estimated using optical images was ~ 300 μm^2. At least three independent batches of samples

were prepared and 6 - 7 junctions were measured on each sample to obtain reasonably statistically significant averages. On each junction we measured 20 scans within a bias range of ± 1 *V*. The total number of measured junctions was ~ 18 - 20 and the total number of J-V curves was around 400 - 450. (Experiential currents were normalized using geometrical contact areas to obtain *J-V* data and were not corrected for effective contact area of junctions, as recent reports demonstrate that effective contact area is 10^{-4} times lower than geometrical contact area)(Weiss et al., 2007; Rothemund et al., 2018; Simeone et al., 2013)

(II) PDMS Microchannel E-GaIn contacts (with ^{TS}Au substrate)

E-GaIn inside a PDMS microchannel (~50 μm channel width) configuration as discussed in the article (figure - 4) was utilized for electrical measurement across protein monolayers on stripped gold substrates (~ 10 μm).

We estimated geometric area of the junction was ~ 500 μm^2. Measurements were carried out with at least three independent samples and 4 - 5 junctions on each sample. At WIS, on each junction, 10 current-voltage sweeps were recorded within a bias range of ± 0.5 *V*. The total number of measured junctions was ~ 20 and the total number of *I-V* curves was 60. AT NUS the same device configuration and measurement protocol was followed but the voltage sweeps were in the bias range of ± 1*V*. The total number of measured junctions was ~ 20 and total number of *J-V* curves was ~ 420.

(III) Hg-drop contact (with Si/SiO_x substrate)

Current-voltage measurements were carried out *in a* dry N_2 *environment* at < 15% humidity *for* 6-8 junctions (on 1 cm x 1 cm sample size) *for* each of 3 different batch of samples (total *number of* junctions ~ 20). Each junction was measured five times *over a* bias range of ± 1 V starting from 0 V.

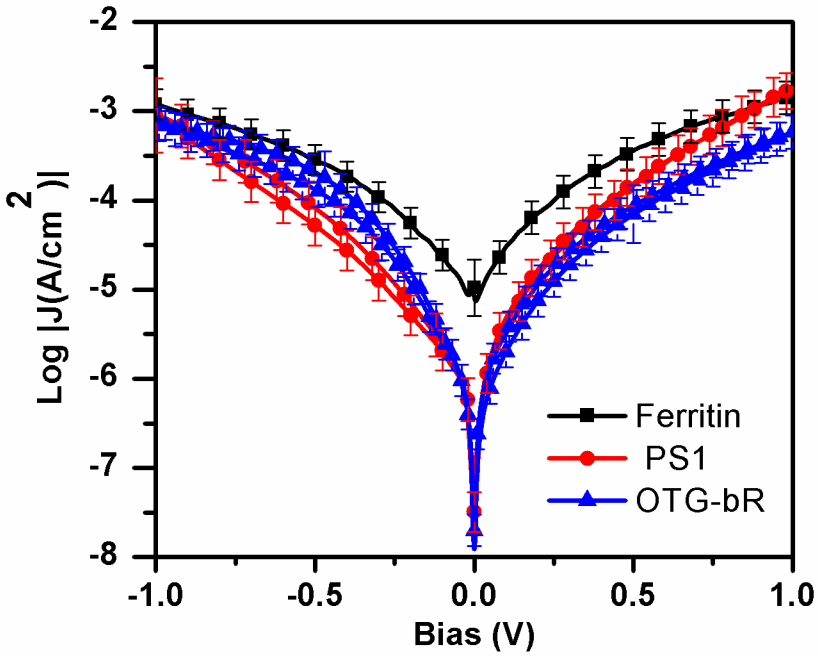

Figure S10. Related to Figure 4 - Room temperature current density-voltage (*J-V*) characteristics: Room temperature *J-V* curves with the three proteins on APTM- treated Si substrates with hanging Hg drop as top electrode. The plots show data that were averaged over 20 junctions from 4 different samples.

(IV) Lift-off-Float-On (Au-LOFO) contact (with Si/SiO_x substrate)

Electrical measurements were carried out in in vacuum at pressure 10^{-2} mbar as well as 10^{-4} mbar. No significant differences were observed between current measurements at these different pressures.

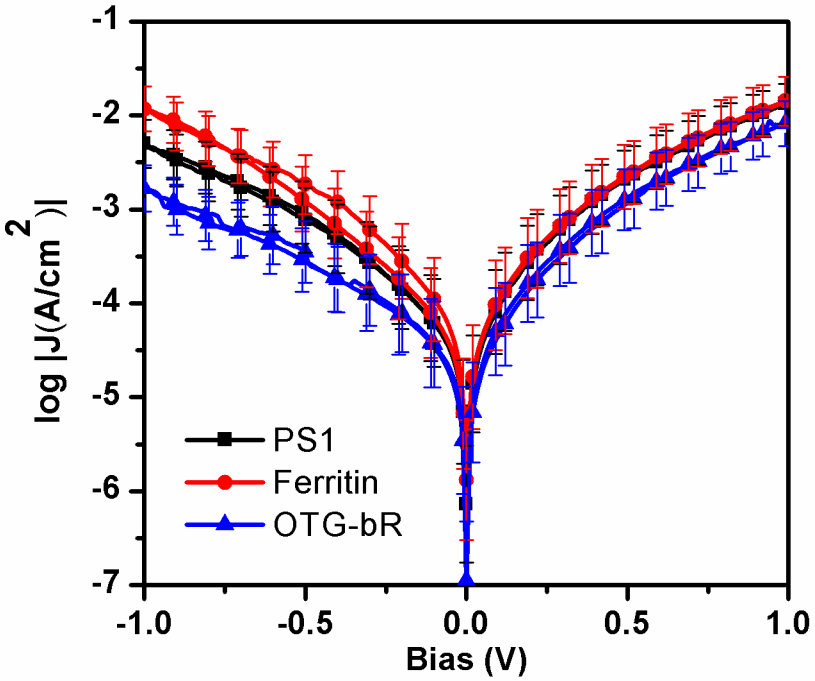

Figure S11. Related to Figure 4 - Room temperature current density-voltage (*J-V*) characteristics: Room temperature *J-V* measurements of Ferritin, PSI monolayers and OTG-bR film on Si substrate with Au-LOFO as top contact. Average current and current density were calculated over 12 different Au-LOFOs on 4 different batches of samples for Ferritin; over 8 different Au-LOFOs on 3 different batches of samples for PSI; and 15 different LOFOs on 6 different batches of samples for OTG-bR.

(V) Corrected current density (A/cm^2) utilizing A_{elec}/A_{geo} ratio

The uncertainties in the A_{elec} all measurement techniques with EGaIn top electrode varies with junction geometry and electronic molecule-electrode coupling, and accurate corrected factors were obtained from our earlier in works (Chen et al., 2019; Kumar et al., 2016; Wan et al., 2014). EGaIn stabilized in a microchannel (µch-EGaIn), A_{elec}/A_{geo} correction factors was 50. A_{elec}/A_{geo} ratio for ^{TS}Au-linker-protein//GaO_x/th-EGaIn was 10^3 , whereas A_{elec}/A_{geo} ratio for ^{TS}Au-linker-protein//GaO_x/tip-EGaIn configuration was 10^4.(Chen et al., 2019; Kumar et al., 2016; Wan et al., 2014) Once experimental current density-voltage (*J-V*) data was corrected for A_{elec}/A_{geo}, all *J-V* data falls within one order of magnitude variations as in the figure (Fig. S18). Bacteriorhodopsin proteins demonstrated much higher current density with ^{TS}Au-linker-protein//GaO_x/th-EGaIn junction configuration, that could be originated from the higher compression force to the protein layer in this configuration, where a transition from reversible to irreversible conformation alteration was occurred, inducting e-transport at higher tunneling rate.(Mukhopadhyay et al., 2014)

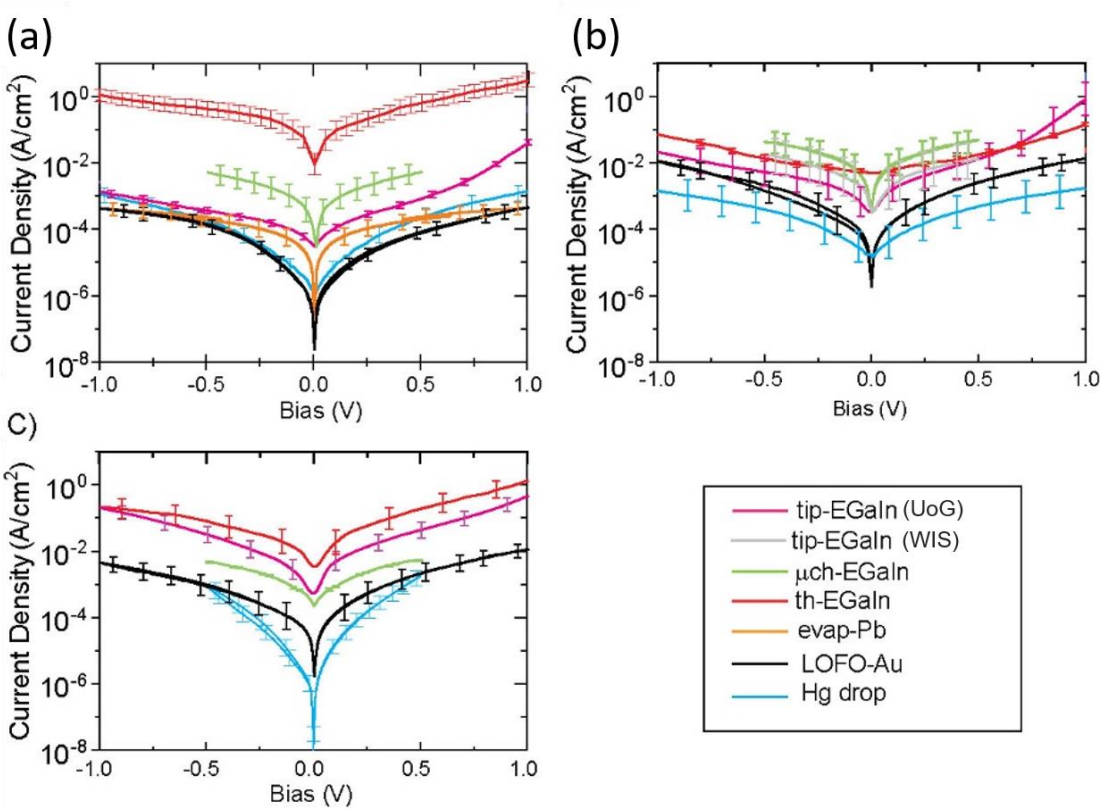

Figure S12. Related to Figure 4: Corrected current density (A/cm2) vs. voltage (*J*-*V*) data for different junction configurations with the A_{elec}/A_{geo} ratio (a) OTG-bacteriorhodopsin (bR), (b) ferritin, and (c) photosystem I (PSI).

(VI) Electrical measurements with nanoscopic junction

Suspended-nanowire" technique provides new methodology for *I*–*V* measurements across protein monolayers without damaging the protein, *i.e.*, electrical contacts have to be nondestructive. Covalently coupled protein monolayer on pre-patterned Au microelectrodes was used suspended nanowire technique. Au nanowires, ~300 nm in diameter and ~4 μm long, were trapped di-electrophoretically onto the electrodes before 8-10 hours of electrical measurements and further dried in N_2 box until the measurements. Since the yield of trapping was only ~ 20%, it was rare that two or more Au nanorod bridged two contact pads. We have used optical microscopy to easily detect proper junctions prior to electronic transport measurements. Next, the devices were loaded on an electrically floating sample stage and were placed in a cryogenic Lakeshore probe station (TTPX). *I*–*V* measurements were performed across protein monolayers, using a Keithley 6430 Sub-Femto amp Source-Meter, with a voltage scan rate of 20 mV s^{-1} in a vacuum of 10^{-2} mbar. For all measurements, a specific side of the junction was grounded, while the other one was biased, in a consistent manner (in order to ensure that the bias polarity was in the same direction for all measurements). In each set of experiments, scans were acquired that started and ended at 0 *V* (*i.e.*, voltage sweep was 0 → −0.3 *V*, −0.3 *V*→ 0.3 *V*, 0.3 *V* → 0 *V*), to check if features in the *I*–*V* behavior originate from the polarity of the initial voltage that is applied and from the scan direction (hysteresis check).

In Table S1 we summarize the number and types of experiments done in different laboratories with different junction configurations:

Table S1. Related to Figure 4: List of number of independent junction preparations and repeating scans for statistical analyses[1]

Table – S1				
Junctions description	NUS	WIS	UoG	UoA
Si/SiO_x-linker-protein//LOFO-Au	NA	# of Junctions ~ 20; 5 *I-V* scans / junction	NA	NA
Si/SiO_x-linker-protein//Hg	NA	# of Junctions ~ 20; 5 *I-V* scans / junction	NA	NA
Au-Linker-protein//Au nanowire	NA	# of Junctions ~ 10; 5 *I-V* scans / junction	NA	NA
Si/SiO_x-linker-protein// evap-Pb/Au	NA	# of Junctions ~ 10; 5 *I-V* scans / junction	NA	NA
^{TS}Au-linker-protein//GaO_x/ th-EGaIn	# of Junctions ~ 20; 20 *I-V* scans / junction	NA	# of Junctions ~ 20; 20 *I-V* scans / junction	NA
^{TS}Au-linker-protein//GaO_x/ µch-EGaIn	# of Junctions ~ 20; 20 *I-V* scans / junction	# of Junctions 10; 10 *I-V* scans / junction	# of Junctions ~ 20; 20 *I-V* scans / junction	NA
^{TS}Au-linker-protein//GaO_x/ tTip-EGaIn	# of Junctions ~ 20; 20 *I-V* scans / junction	# of Junctions ~ 50; 5 *I-V* scans / junction	# of Junctions ~ 20; 20 *I-V* scans / junction	NA
Carbon-NAB//e-C//Au	# of Junctions 7; 20 *I-V* scans / junction	# of Junctions 7; 5 *I-V* scans / junction	# of Junctions 7; 20 *I-V* scans / junction	# of Junctions 7; 10 *I-V* scans / junction
Carbon-NAB//e-C//GaO_x/ Tip-EGaIn	# of Junctions ~ 20; 20 *I-V* scans / junction	NA	NA	NA

[1] In our statistical analyses we used the arithmetic mean of the *J*-V sets for graphical use; transport parameters were obtained by numerical fitting of individual *J*-V sets.

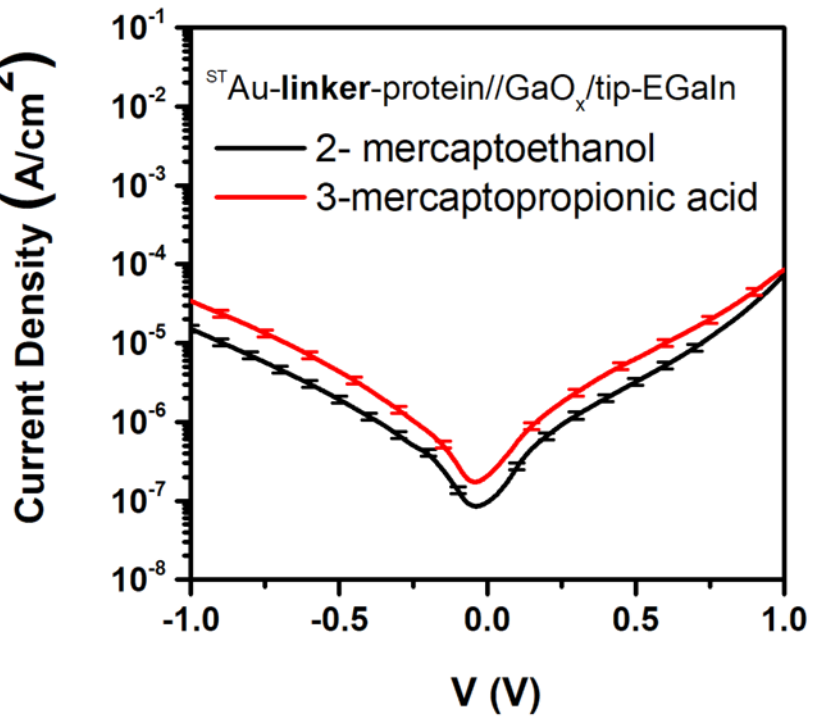

Figure S13. Related to Figure 4 and Role of the Linker: Effect of varying linker on current densities across PSI monolayer with linker designated in figure. The two linkers in were reported to invert the PSI orientation due to surface charge of the linker layer.

4. Temperature-Dependent Electrical Measurements

At WIS a vacuum (10^{-4} mbar) chamber in a 90 TTPX cryogenic 4-probe electrical measurement probe station (Lakeshore Inc.) was used for temperature-dependent measurements. For measurements with LOFO Au as top contacts, the Si substrate was electrically grounded to a metal substrate holder (using conductive silver paint). Soft gold wire (25μm diameter) was connected to metal probes of probe stations to serve as gentle electrical contact to LOFO Au pads. Both the sample holder and the probes were cooled using liquid N_2. The temperature was controlled and monitored with an accuracy of 0.2 K (Lakeshore controller 336).

For the PDMS microfluidic channel device configuration a VRX-VF cryogenic electrical measurement probe station (Lakeshore Inc.) was utilized for the temperature dependent measurements at NUS. Microfluidic chips filled with EGaIn were first kept on protein monolayer on glass supported ^{TS}Au substrate, then whole device was transferred inside the probe station. Electrical probes were directly connected to the ^{TS}Au bottom contact pad and top EGaIn drop for current-voltage measurements at various temperatures.

Section B.

1. Effect of the linker and protein orientation on Electrical transport

Electron transport across protein monolayers get effected by protein's orientation, as well as the linker we used to tether protein to metal electrodes. In comparison study, we have utilized Ferritin, OTG-bacteriorhodopsin (bR), photosystem I (PSI) protein monolayers. For orientation dependent electron transport studies, we have excluded the ferritin monolayers, owing to the circular symmetrical globular tertiary nature of that protein.

bR as a membrane protein, re-embedded with its lipids into a detergent film, has only two possible orientations. bR bilayers were prepared by adsorbing freshly prepared octylthioglucoside (OTG) vesicles on linker-modified Si/SiO_x or ^{TS}Au substrate. Both fusion into a monolayer and vesicle collapse to yield a bilayer can occur. The inside-out orientation of the bR protein in vesicles implies that, whenever the layer forms from the vesicle, the bR is always oriented with its Cytoplasmic side (CP) facing the substrate, irrespective of the linker that is used.(Jin et al., 2007).

Also PSI is a membrane protein, and has only 2 possible orientations. Here those can be selected or at least preferred by using different linkers to Au substrates.

Thus, the nature of the used proteins and modification of electrodes with linker molecules limit the number of possible orientations that we can have.

There are very few published reports (Amdursky et al., 2014; Fereiro et al., 2019; Garg et al., 2018) where theoretical calculations added insights into orientations of protein films, through which electron transport was measured.

Amongst the large number of tested junctions, we repeated two, viz. ^{TS}Au-linker-protein//GaO_x/µch-EGaIn and ^{TS}Au-linker-protein//GaO_x/tip-EGaIn, using two different linkers to ensure different orientations.

In our measurements, as well as those reported before, the effect of varying linkers of similar length is orders of magnitude smaller than that of the junction preparation method / contacting configuration.

2. Comparison of current density with PDMS stamp and cone shaped EGaIn junction devices

In self-assembled molecular junction, device current directly intent by the actual contact area between electrodes and self-assembled monolayers. The variation between actual contact area and experimentally measured contact area or geometrical contact area mostly originate from top-electrode. In order to quantify this variation, we have studied molecular junction prepared by E-GaIn top electrode with PDMS microchannel and cone shaped EGaIn drop prepared at top of the needle. We have statistically compared voltage-current behavior of molecular junctions made of SC10 alkanethiolate SAM on stripped gold electrodes with above-mentioned EGaIn as top electrode methods. Cone shaped EGaIn is utilized as routinely fabricated in different laboratories and microchannel PDMS stamp methods developed at NUS and distributed over laboratories. The statistical summary of J-V characteristics demonstrate that current density from cone shaped EGaIn is always

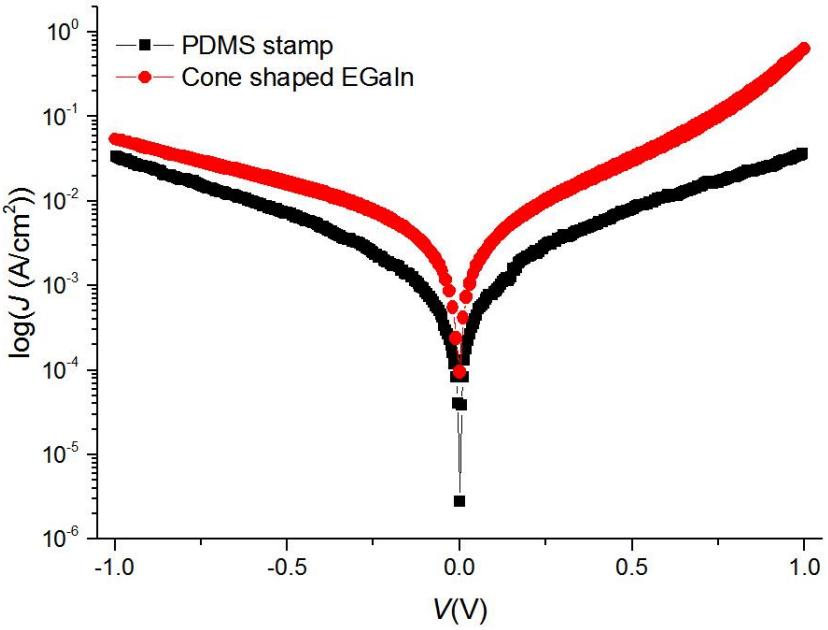

Figure S14. Related to Figure 4: Plots of log*J* versus *V* for junctions with SC_{10} alkanethiolate SAM measured with th-EGaIn devices and tip-EGaIn as a top-electrode at room temperature.

3. Extraction of Numerical Parameters from the Current – Voltage Response

3a. Parameters extraction from fitting to parabolic approximation (Equation 1 of main text)

In contrast to Equation 1 (main text), the parabolic model was not fitted to the *J*-*V* data directly, but rather to its normalized differential conductance: $NDC = \frac{d\log I}{d\log V}$. This presentation eliminates the linear growth ($G_{eq} \cdot V$) and by that magnifies the deviation from this standard background.(Vilan, 2017) This is important for few reasons: first, it reduces the number of fitting parameters from three to two: only V_0 and S. Second, the 'log-like' scaling reduces the over-emphasis to high signals that is inherent to least-errors numerical fitting procedures. Finally, NDC gives direct feedback on the "legit" fitting range: the three-terms Taylor expansion (equation 1, main text) cannot reach NDC > 3. Therefore our fitting procedure was limited to measured values with NDC ≤ 3.

Applying the NDC function ($\frac{d\log I}{d\log V}$) to the parabolic approximation (Eq. 1, main text) yields the following expression:

$$NDC_{Parb} = 2 + \frac{V^2 - V_0^2}{V_0^2 + SV_0V + V^2} \qquad \text{(Eq. S1)}$$

The fitting of Eq. S1 to a given set of NDC vs. voltage curves was performed with the 'fit.m' function of MatLab, using 'Bisquare' robust fitting. This gave the parameters V_0 and S, and their errors are the 95% confidence level in the extracted parameters.

The third parameter, G_{eq}, was extracted from the mean ratio between the measured conductance ($G = \frac{dJ}{dV}$) and the parabolic approximation ($1 + 2S\,V_i/V_0 + 3(V_i/V_0)^2$):

$$G_{eq} = \frac{1}{n}\sum_{i=1}^{n} \frac{G_i}{1 + 2SV_i/V_0 + 3(V_i/V_0)^2} \qquad \text{(Eq. S2)}$$

Only data points that comply with the criterion: $1 \leq NDC_i \leq 3$ were included in the averaging of Eq. S2. The error in G_{eq} is the standard deviation in the log of the ratio in Eq. S2.

As a routine, equation 1 (main text) is fitted also to G-V and J-V presentations. In general, parameters extracted by G-V procedure were rather similar to those from NDC-V, with less than 10% variation for most junctions. The fit to J-V presentation gave larger deviations, which we attribute to over-emphasis of the high-signals, against the notion of near-zero expansion. Finally, a direct extraction of G_{eq} from the slope of J vs. V in the close vicinity of zero V (4 data points on each side of 0 V) also revealed good agreement with the values extracted by Eq. S2.

3b. Parameter extraction by transition voltage spectroscopy (TVS):

In order to support the physical validity of the energy-barrier values (Table 3, main text), we have also run an alternative method known as transition voltage spectroscopy (TVS).(Bâldea, 2012) Traditionally, TVS searches for the voltage, V_t where the function $\ln|I/V^k|$ has a minimum ($k > 1$). Mathematically this is identical(Vilan, 2017) to searching the voltage where $NDC = k$, designated as $V_k^{+,-}$, where ± marks the bias polarity. It is common to take $k = 2$, though in practice not all traces reach $NDC = 2$, and then TVS is extracted at $1 < k < 2$. Notice though that the choice of k often has a large effect on the extracted ε_0 value. The translation of $V_k^{+,-}$ to energy barrier, ε_0, and partition factor, α, is derived from the sum ($\Sigma = V_k^+ + V_k^-$) and the product ($\Pi = |V_k^+ \cdot V_k^-|$) of transition voltage values at the two bias polarities:(Bâldea, 2012)

$$\varepsilon_0 = \frac{k}{k-1} \cdot \frac{q\Pi}{\sqrt{\Sigma^2 + \Pi \cdot 4/(1-k^{-2})}} \qquad \text{(Eq. S3)}$$

$$\alpha = \frac{\Sigma}{2\sqrt{\Sigma^2 + \Pi \cdot 4/(1-k^{-2})}} \qquad \text{(Eq. S4)}$$

Notice, that $V_k^+ > 0$ while $V_k^- < 0$, such that in a symmetric case, $\Sigma = 0$. In addition, the elementary charge, $q = 1[eV/V]$.

Within this 'transition' approach, the third parameter, G_{eq} value is extracted from the so-called(Bâldea et al., 2015) 'critical current' or the current at the k transition point:

$$G_{eq} = \frac{I_k}{V_k}(1 + 2\alpha\, qV_k/\varepsilon_0 - (0.25 - \alpha^2)(qV_k/\varepsilon_0)^2) \qquad \text{(Eq. S5)}$$

The derivation was repeated for both positive and negative sets of (V_k, I_k) and reported value is their geometrical average;

3c. Summary of various extracted parameters

Table S2. Related to Figure 7 and Table 3: Extracted empirical parameters (G_{eq}, V_0, S) and their translation into single-level physical values (Γ. ε_0. α), using either parabolic fitting (Fit[a]) or threshold method (TVS[b]).

Protein:	Ferritin	Footprint:	60							
Configuration[c]	G_{eq} [μS/cm^2]	Coupling[d] G_{eq} [μS/cm^2]	Γ [neV]	V_0 [V]	Potential ε_0 [eV]	ε_0 [eV] (*k*)	S	α[e]	Asymmetry α	RR[f]
	Fit	TVS	Fit	Fit	Fit	TVS	Fit	Fit	TVS	raw
UoG	1.1 ± 79%	0.93	20 ± 58%	0.39 ± 19%	0.33 ± 19%	0.43 (2.0)	-1.42 ± 53%	0.50	-0.118	59.08
NUS	1.2 ± 39%	1.24	26 ± 40%	0.48 ± 20%	0.41 ± 20%	0.38 (2.0)	0.79 ± 104%	-0.27	0.019	2.21
EGaIn Cone	2.7 ± 4.8%	2.71	59 ± 8%	0.71 ± 6%	0.87 ± 89%	0.30 (1.3)	-0.47 ± 41%	0.13	-	0.66
EGaIn μch	970 ± 11%	942	1690 ± 11%	1.07 ± 6%	0.94 ± 12%	0.48 (1.3)	-0.13 ± 75%	0.03	0.023	0.87
Si/ Au(LOFO)	830 ± 18%	916	390 ± 10%	0.27 ± 1%	0.44 ± 52%	0.16 (1.5)	0.57 ± 10%	-0.16	-0.070	1.25
Si/ Hg Drop	325 ± 20%	252	520 ± 18%	0.57 ± 8%	0.49 ± 19%	0.24 (1.8)	0.06 ± 650%	-0.02	-0.024	1.23

Protein:	Photosyst. 1	Footprint:	140							
Configuration[c]	G_{eq} [μS/cm^2]	Coupling[d] G_{eq}[μS/cm^2]	Γ [neV]	V_0 [V]	Potential ε_0 [eV]	ε_0 [eV] (*k*)	S	α[e]	Asymmetry α	RR[f]
	Fit	TVS	Fit	Fit	Fit	TVS	Fit	Fit	TVS	raw
UoG, 2ME	2.21 ± 44%	2.07	27 ± 39%	0.36 ± 17%	0.31 ± 17%	0.28 (1.5)	0.77 ± 82%	-0.26	-0.009	4.8
UoG, MPS	3.88 ± 31%	4.60	33 ± 28%	0.33 ± 13%	0.19 ± 97%	0.31 (2.0)	0.61 ± 76%	-0.18	0.050	2.5
NUS	20.5 ± 15%	25.8	113 ± 15%	0.49 ± 8%	0.29 ± 59%	0.44 (2.0)	0.62 ± 44%	-0.19	0.004	7.9
WIS EGaIn	153 ± 13%	174	340 ± 12%	0.54 ± 6%	0.47 ± 6%	0.39 (1.3)	0.01±1430%	-0.002	-0.102	1.2
Si/ Au(LOFO)	653 ± 25%	728	396 ± 15%	0.30 ± 3%	0.32 ± 37%	0.17 (1.5)	0.38 ± 35%	-0.10	-0.121	2.7

Protein:	OTG-bR	Footprint:	80							
		Coupling[d]			Potential				Asymmetry	

Configuration[c]	G_{eq} [mS/cm^2]	G_{eq}[mS/cm^2]	Γ [μeV]	V_0 [V]	ε_0 [eV]	ε_0 [eV] (k)	S	α[e]	α	RR[f]
	Fit	TVS	Fit	Fit	Fit	TVS	Fit	Fit	TVS	raw
UoG	0.0005 ± 20%	0.0004	0.02 ± 34%	0.67 ± 24%	0.58 ± 24%	0.43 (2.0)	0.99 ± 65%	-0.47	-0.12	43.4
NUS cysteamine	1.31 ± 29%	1.01	1.6 ± 27%	0.86 ± 12%	0.74 ± 12%	0.53 (1.5)	1.22 ± 30%	-0.50	-0.15	3.15
NUS 6-amino	13.7 ± 18%	13.9	4.7 ± 21%	0.79 ± 12%	0.79 ± 110%	0.43 (1.5)	0.60 ± 93%	-0.17	-0.17	3.15
Au-EGaIn	0.45 ± 7%	0.46	0.75 ± 6%	0.70 ± 3%	0.61 ± 7%	0.42 (1.3)	0.11 ± 66%	-0.03	-0.032	1.04
Lead	0.21 ± 22%	0.20	0.25 ± 15%	0.34 ± 4%	0.30 ± 18%	0.17 (1.5)	-0.15 ± 130%	0.04	0.084	0.82
Si/ Au(LOFO)	0.10 ± 36%	0.11	0.07 ± 22%	0.14 ± 4%	0.24 ± 33%	0.10 (1.5)	0.57 ± 29%	-0.16	0.012	1.09

a) **Fit** refers to fitting equation S1 to an NDC presentation of averaged *J-V* sets after smoothing; $\mathbf{G_{eq}}$ values were extracted using equation S2.
b) Although majority of the traces have reached NDC = 2, $\boldsymbol{k} < 2$ was often chosen to avoid the region where NDC saturates.(Vilan, 2017) The value of $\boldsymbol{k}$ is given in brackets in the ε_0/**TVS** column.
c) Configuration column gives a short-hand description: **UoG**, **NUS**: these two labs have used different variants of ^{TS}Au/EGaIn as detailed in the main text. **Si** refers to the silicon wafers, in contrast to all other cases which haves used Au substrates. All other information specifies different forms of top-contacts, all prepared by by WIS lab.
d) Notice the difference in unit scales: G_{eq} is in micro (10^{-6}) and Γ is in nano (10^{-9}) for Ferritin and phosotsystem1 while for OTG-bR these values are 1000 times larger, in milli (10^{-3}) and micro (10^{-6}), respectively,
e) The error in α, in percentage is almost identical to that in *S*, and therefore omitted.
f) RR is the rectification ratio that is the ratio between the currents at ±1V; in few cases were the highest voltage was less than |1|V, the RR ratio was taken at the maximal signal.

Supplemental References:

Amdursky, N., Ferber, D., Bortolotti, C.A., Dolgikh, D.A., Chertkova, R.V., Pecht, I., Sheves, M., and Cahen, D. (2014). Solid-state electron transport via cytochrome c depends on electronic coupling to electrodes and across the protein. Proc Natl Acad Sci U A *111*, 5556–5561.

Bâldea, I. (2012). Ambipolar transition voltage spectroscopy: Analytical results and experimental agreement. Phys. Rev. B *85*, 035442.

Bâldea, I., Xie, Z., and Frisbie, C.D. (2015). Uncovering a law of corresponding states for electron tunneling in molecular junctions. Nanoscale *7*, 10465–10471.

Castañeda Ocampo, O.E., Gordiichuk, P., Catarci, S., Gautier, D.A., Herrmann, A., and Chiechi, R.C. (2015). Mechanism of Orientation-Dependent Asymmetric Charge Transport in Tunneling Junctions Comprising Photosystem I. J Am Chem Soc *137*, 8419–8427.

Chen, X., Hu, H., Trasobares, J., and Nijhuis, C.A. (2019). Rectification Ratio and Tunneling Decay Coefficient Depend on the Contact Geometry Revealed by in Situ Imaging of the Formation of EGaIn Junctions. ACS Appl. Mater. Interfaces *11*, 21018–21029.

Fereiro, J.A., Kayser, B., Romero-Muñiz, C., Vilan, A., Dolgikh, D.A., Chertkova, R.V., Cuevas, J.C., Zotti, L.A., Pecht, I., Sheves, M., et al. (2019). A Solid-State Protein Junction Serves as a Bias-Induced Current Switch. Angew. Chem. Int. Ed. *58*, 11852–11859.

Garg, K., Raichlin, S., Bendikov, T., Pecht, I., Sheves, M., and Cahen, D. (2018). Interface Electrostatics Dictates the Electron Transport via Bioelectronic Junctions. ACS Appl Mater Interfaces *10*, 41599–41607.

Jin, Y., Friedman, N., Sheves, M., He, T., and Cahen, D. (2006). Bacteriorhodopsin (bR) as an Electronic Conduction Medium: Current Transport through bR-Containing Monolayers. Proc Natl Acad Sci U A *103*, 8601–8606.

Jin, Y., Honig, T., Ron, I., Friedman, N., Sheves, M., and Cahen, D. (2008). Bacteriorhodopsin as an electronic conduction medium for biomolecular electronics. Chem. Soc. Rev. *37*, 2422–2432.

Jin, Y.D., Friedman, N., Sheves, M., and Cahen, D. (2007). Bacteriorhodopsin-Monolayer-Based Planar Metal–Insulator–Metal Junctions via Biomimetic Vesicle Fusion: Preparation, Characterization, and Bio-optoelectronic Characteristics. Adv Funct Mater *17*, 1417–1428.

Kommareddy, K.P., Lange, C., Rumpler, M., Dunlop, J.W.C., Manjubala, I., Cui, J., Kratz, K., Lendlein, A., and Fratzl, P. (2010). Two stages in three-dimensional in vitro growth of tissue generated by osteoblastlike cells. Biointerphases *5*, 45–52.

Kumar, K.S., Pasula, R.R., Lim, S., and Nijhuis, C.A. (2016). Long-Range Tunneling Processes across Ferritin-Based Junctions. Adv. Mater. *28*, 1824–1830.

Mukhopadhyay, S., Cohen, S.R., Marchak, D., Friedman, N., Pecht, I., Sheves, M., and Cahen, D. (2014). Nanoscale Electron Transport and Photodynamics Enhancement in Lipid-Depleted Bacteriorhodopsin Monomers. ACS Nano *8*, 7714–7722.

Rothemund, P., Morris Bowers, C., Suo, Z., and Whitesides, G.M. (2018). Influence of the Contact Area on the Current Density across Molecular Tunneling Junctions Measured with EGaIn Top-Electrodes. Chem. Mater. *30*, 129–137.

Salomon, A., Cahen, D., Lindsay, S., Tomfohr, J., Engelkes, V.B., and Frisbie, C.D. (2003). Comparison of Electronic Transport Measurements on Organic Molecules. Adv Mater *15*, 1881–1890.

Simeone, F.C., Yoon, H.J., Thuo, M.M., Barber, J.R., Smith, B., and Whitesides, G.M. (2013). Defining the Value of Injection Current and Effective Electrical Contact Area for EGaIn-Based Molecular Tunneling Junctions. J Am Chem Soc *135*, 18131–18144.

Vilan, A. (2017). Revealing tunnelling details by normalized differential conductance analysis of transport across molecular junctions. Phys. Chem. Chem. Phys. *19*, 27166–27172.

Wan, A., Jiang, L., Sangeeth, C.S.S., and Nijhuis, C.A. (2014). Reversible Soft Top-Contacts to Yield Molecular Junctions with Precise and Reproducible Electrical Characteristics. Adv. Funct. Mater. *24*, 4442–4456.

Weiss, E.A., Chiechi, R.C., Kaufman, G.K., Kriebel, J.K., Li, Z., Duati, M., Rampi, M.A., and Whitesides, G.M. (2007). Influence of Defects on the Electrical Characteristics of Mercury-Drop Junctions: Self-Assembled Monolayers of n-Alkanethiolates on Rough and Smooth Silver. J. Am. Chem. Soc. *129*, 4336–4349.